Regolith production and transport at the Susquehanna Shale Hills Critical Zone Observatory, Part 2: Insights from meteoric ^{10}Be

Nicole West,[1] Eric Kirby,[1,2] Paul Bierman,[3] Rudy Slingerland,[1] Lin Ma,[4] Dylan Rood,[5,6] and Susan Brantley[1]

Received 11 January 2013; revised 23 July 2013; accepted 23 July 2013.

[1] Regolith-mantled hillslopes are ubiquitous features of most temperate landscapes, and their morphology reflects the climatically, biologically, and tectonically mediated interplay between regolith production and downslope transport. Despite intensive research, few studies have quantified both of these mass fluxes in the same field site. Here we present an analysis of 87 meteoric ^{10}Be measurements from regolith and bedrock within the Susquehanna Shale Hills Critical Zone Observatory (SSHO), in central Pennsylvania. Meteoric ^{10}Be concentrations in bulk regolith samples ($n = 73$) decrease with regolith depth. Comparison of hillslope meteoric ^{10}Be inventories with analyses of rock chip samples ($n = 14$) from a 24 m bedrock core confirms that >80% of the total inventory is retained in the regolith. The systematic downslope increase of meteoric ^{10}Be inventories observed at SSHO is consistent with ^{10}Be accumulation in slowly creeping regolith (~ 0.2 cm yr^{-1}). Regolith flux inferred from meteoric ^{10}Be varies linearly with topographic gradient (determined from high-resolution light detection and ranging-based topography) along the upper portions of hillslopes at SSHO. However, regolith flux appears to depend on the product of gradient and regolith depth where regolith is thick, near the base of hillslopes. Meteoric ^{10}Be inventories at the north and south ridgetops indicate minimum regolith residence times of 10.5 ± 3.7 and 9.1 ± 2.9 ky, respectively, similar to residence times inferred from U-series isotopes in Ma et al. (2013). The combination of our results with U-series-derived regolith production rates implies that regolith production and erosion rates are similar to within a factor of two on SSHO hillcrests.

Citation: West, N., E. Kirby, P. Bierman, R. Slingerland, L. Ma, D. Rood, and S. Brantley (2013), Regolith production and transport at the Susquehanna Shale Hills Critical Zone Observatory, Part 2: Insights from meteoric ^{10}Be, *J. Geophys. Res. Earth Surf.*, *118*, doi:10.1002/jgrf.20121.

1. Introduction

[2] The physical and chemical transformation of bedrock to regolith is fundamental to the functioning and evolution of the Critical Zone, the region extending from the tree canopy to the deepest reaches of groundwater [*Brantley et al.*, 2007; *Anderson et al.*, 2007; *Amundson et al.*, 2007; *Brantley and White*, 2009]. Much of this transformation occurs during the development and transport of regolith in the upper meters of the Earth's surface. Regolith production influences the chemistry of surface waters and buffers atmospheric CO_2 concentrations through consumption and burial of carbon during silicate weathering [*Raymo and Ruddiman*, 1988, 1992; *Gaillardet et al.*, 1999], and the physical breakdown of rock to mobile regolith strongly influences the rates of sediment delivery to basins [e.g., *Willenbring and von Blanckenburg*, 2010a]. Chemical and physical weathering are strongly coupled [*Riebe et al.*, 2003], as mechanical breakdown of rock leads to a fresh supply of readily weatherable material [*Stallard and Edmond*, 1983]. It is well understood that the mass balance of regolith on soil-mantled hillslopes is governed by a competition between regolith production via weathering, mass lost by dissolution, and the divergence of mobile regolith flux [e.g., *Gilbert*, 1909; *Kirkby*, 1971]. The dependence of these processes on the interplay among hillslope hydrology [*Dunne*, 1998], biota [*Moulton and Berner*, 1998; *Roering et al.*, 2010; *Gabet and Mudd*, 2010], climate [*Millot et al.*, 2002; *Riebe et al.*, 2003; 2004], and tectonics [*Riebe et al.*, 2001; *Heimsath et al.*, 2012], however, makes predicting

[1]Earth and Environmental Systems Institute and Department of Geosciences, Pennsylvania State University, University Park, Pennsylvania, USA.
[2]Now at College of Earth, Ocean and Atmospheric Sciences, Oregon State University, Corvallis, Oregon, USA.
[3]Geology Department, University of Vermont, Burlington, Vermont, USA.
[4]Department of Geological Sciences, University of Texas, El Paso, Texas, USA.
[5]AMS Laboratory, Scottish Universities Environmental Research Centre, East Kilbride, UK.
[6]Earth Research Institute, University of California, Livermore, California, USA.

Corresponding author: N. West, Earth and Environmental Systems Institute and Department of Geosciences, Pennsylvania State University, 542 Deike Building, University Park, PA 16802, USA. (nxw157@psu.edu)

2169-9003/13/10.1002/jgrf.20121

the evolution of regolith over time challenging [*Dietrich et al*., 2003; *Anderson et al*., 2007].

[3] In the past two decades, the application of novel isotopic techniques to the study of earth surface processes [e.g., *Pavich et al*., 1985; *Lal*, 1991; *Brown et al*., 1995; *Gosse and Phillips*, 2001; *Granger*, 2006; *Chabaux et al*., 2008; *Dosseto et al*., 2008] has allowed, for the first time, direct measurement of the rates of mass fluxes on eroding hillslopes. The accumulation of meteoric ^{10}Be in regolith can be a tracer of regolith residence time [*Pavich et al*., 1986] as well as downslope mobile regolith flux [*McKean et al*., 1993; *Jungers et al*., 2009], whereas the concentration of in situ ^{10}Be in weathered bedrock at the base of regolith can constrain rates of regolith production on eroding hillslopes [*Heimsath et al*., 1997; *Small et al*., 1999; *Heimsath et al*., 2012]. Similarly, the fractionation of uranium-series isotopes during weathering provides constraints on regolith production [*Chabaux et al*., 2008; *Dosseto et al*., 2008; *Ma et al*., 2010].

[4] Application of these chronologic techniques has confirmed several key notions of landscape evolution [*Gilbert*, 1909; *Ahnert*, 1987], including the suggestion that rates of regolith production depend on regolith thickness [*Small et al*., 1999; *Heimsath et al*., 1999] and that downslope transport by creep depends on both hillslope gradient [*Roering*, 2008] and regolith depth [*Heimsath et al*., 2005; *Furbish et al*., 2009; *Pelletier et al*., 2011]. Moreover, recent studies have begun to illuminate the linkages between chemical and physical weathering [*Millot et al*., 2002; *Riebe et al*., 2004; *Fletcher et al*., 2006; *Dixon et al*., 2009] and between tectonics and the rate of bedrock weathering [*West et al*., 2005; *Molnar et al*., 2007; *Heimsath et al*., 2012]. Despite these considerable advances, relatively few studies have directly measured fluxes associated with both regolith production and downslope transport in a single field site.

[5] In this study, we exploit the accumulation of meteoric ^{10}Be in regolith and bedrock to determine the residence times and downslope fluxes of regolith within the Susquehanna Shale Hills Critical Zone Observatory (SSHO), a headwater catchment located in the Valley and Ridge Province of central Pennsylvania. In a companion study [*Ma et al*., 2013], we determine soil production rates using uranium-series isotopes in weathered regolith. The SSHO is the focus of ongoing studies of the present-day hydrologic [*Li and Duffy*, 2011] and ecologic [*Naithani et al*., 2010] functioning of regolith, as well as the evolution of regolith over geologic time [*Lin et al*., 2006; *Jin et al*., 2010; *Ma et al*., 2010, 2013; *Lebedeva and Brantley*, 2013]. The novel combination of meteoric ^{10}Be and U-series techniques allows us to independently constrain the timescales of both regolith production and downslope transport on hillslopes in the SSHO and allows us to elucidate geomorphic transport rules that describe regolith flux.

2. Background

2.1. Geologic Setting

[6] The persistence of topography in the Appalachian Mountains has been at the center of a canonical debate over whether or not the Appalachian landscape has reached a state of dynamic equilibrium, where regional landscape metrics such as relief, slope, and elevation fluctuate about some long-term average value [e.g., *Hack*, 1960]. Although this debate is far from settled [*Gallen et al*., 2013; *Miller et al*., 2013; *Rowley et al*., 2013], determinations of short-term erosion rates (~10^4–10^5 year) determined from meteoric [e.g., *Pavich et al*., 1985] and in situ ^{10}Be [e.g., *Matmon et al*., 2003; *Portenga and Bierman*, 2011] are similar to long-term (~10^7–10^8 year) exhumation rates determined using low-temperature thermochronometers [*Spotila et al*., 2004; *Naeser et al*., 2004]. The similarity of erosion rates measured over such widely different timescales suggests that, on average, the topography in the Appalachians has been eroding steadily throughout the Cenozoic [*Matmon et al*., 2003].

[7] Portions of the northern Appalachians, however, were subject to fluctuations in local climatic conditions associated with repeated glaciations during the Late Cenozoic. In central Pennsylvania, widespread deposits of coarse hillslope colluvium and talus fields attest to the efficiency of periglacial frost shattering and solifluction during the recent geologic past [*Clark and Ciolkosz*, 1988; *Braun*, 1989; *Ciolkosz et al*., 1989]. Some suggest that erosion rates near the glacial limit in the Valley and Ridge province of Pennsylvania, ~ 75 km due north of our study area, were enhanced during the marine isotope stage 2 [*Braun*, 1989] and may have exceeded long-term averages for short periods of time.

[8] Presently, the SSHO is located in the Valley and Ridge physiographic province of the Appalachian Mountains and experiences a temperate climate with moderate amounts of rainfall (~1 m/yr) [*NOAA*, 2011]. SSHO is a small catchment (~80,000 m^2) developed on the Silurian Rose Hill Formation, an organic-poor [*Swain*, 1966], Fe-rich [*Meyer et al*., 1992], shale with thin interbedded, fine-grained sandstone, that extends along much of the Appalachians. At SSHO, bedding is oriented NE–SW (N54°E), with dip angles ranging from 25° to 76° to the NW [*Jin et al*., 2010]. The SSHO is a headwater catchment bounded by ridges to the north and south and contains an ephemeral stream that flows west into the Shaver's Creek watershed and eventually joins the Susquehanna River (Figure 1). Near the mouth of the watershed, the ridgelines are nearly perpendicular to bedding strike but become subparallel to bedding near the head of the watershed.

[9] Geomorphic aspects of the SSHO are suggestive of recent changes in sediment flux out of the catchment. Local relief between the valley floor and ridge crests at SSHO is 30 m (Figure 2a). Hillslopes in the SSHO are convex near the ridgetops but are relatively planar along their midslope sections and are characterized by only a few regions of convergent topography ("swales"—Figures 2a and 2b). Hillslope gradients, however, exhibit a pronounced asymmetry; the northern slope has a median gradient of ~15°, whereas the southern slope has a gradient of ~20° (Figures 2c and 2d). Regolith at SSHO is rich in clay, thin at the ridge tops (~30 cm), and thickens downslope [*Lin et al*., 2006; *Jin et al*., 2010]. Deposits along the axis of the valley, and in convergent swales, are significantly thicker and can reach ~ 300 cm along the valley floor [*Lin et al*., 2006]. These thicker deposits appear to be associated with a low (0.5–1 m) fill terrace along the southern valley wall (Figure 1); this surface appears to grade into a ~2–3 m terrace along the eastern valley of the Shaver's Creek trunk

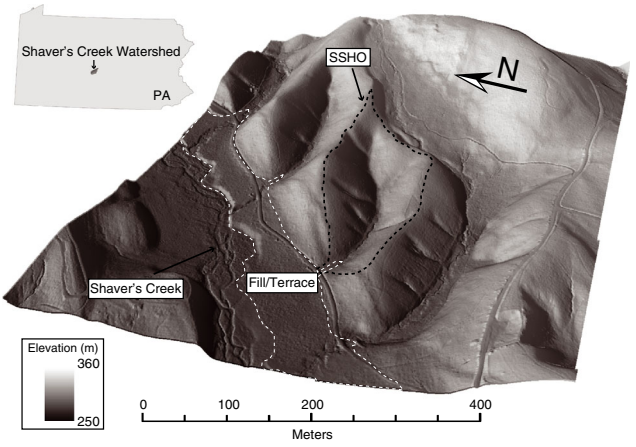

Figure 1. Shaded relief perspective image of the Susquehanna Shale Hills Critical Zone Observatory (SSHO). Image created from high-resolution light detection and ranging (LiDAR) digital elevation data collected in concert with the National Center for Airborne Laser Mapping. The SSHO catchment exhibits relatively low relief and contains a subtle fill terrace into which the present-day channel is incised.

stream (Figure 1). These observations are qualitatively consistent with greater sediment discharges, relative to the transport capacity of the channel, in the recent geologic past. However, the timescales and rates associated with sediment accumulation, and whether they reflect concomitant changes in sediment production on hillslopes, remain uncertain.

[10] Recently, the Shale Hills watershed has been the subject of focused studies on rates of weathering and regolith production. *Jin et al*. [2010] used mass transfer coefficients (τ), a measure of mass balance that normalizes chemical changes relative to an immobile element [*Chadwick et al*., 1990; *Riebe et al*., 2003; *Brantley and White*, 2009], to estimate rates of chemical weathering as well as mass flux values for solutes and sediment on SSHO hillslopes. Analysis of regolith bulk chemistry and comparison to source rock composition suggest progressive loss of major and trace elements away from the regolith-bedrock interface [*Jin et al*., 2010]. *Jin et al*. [2010] relied on a single determination of meteoric ^{10}Be from stream sediment to estimate a basin-average erosion rate for SSHO. These sediments contained an average meteoric ^{10}Be concentration of 3.3×10^8 at g^{-1}, corresponding to a basin-wide erosion rate of ~15 m My^{-1}, a value consistent with the average rates reported for the Appalachians of 17 ± 9 m My^{-1} [*Portenga and Bierman*, 2011].

[11] In a separate study, *Ma et al*. [2010, 2013] exploited the disequilibrium decay of uranium-series isotopes to estimate the timescales associated with weathering at SSHO [e.g., *Chabaux et al*., 2008; *Dosseto et al*., 2008; *Lee et al*., 2010]. Because uranium isotope ratios in regolith reflect the duration of water-rock interactions, they can provide a measure of the time elapsed since rock particles became small enough that decay products were fractionated during weathering [*Chabaux et al*., 2008; *Lee et al*., 2010; *Ma*

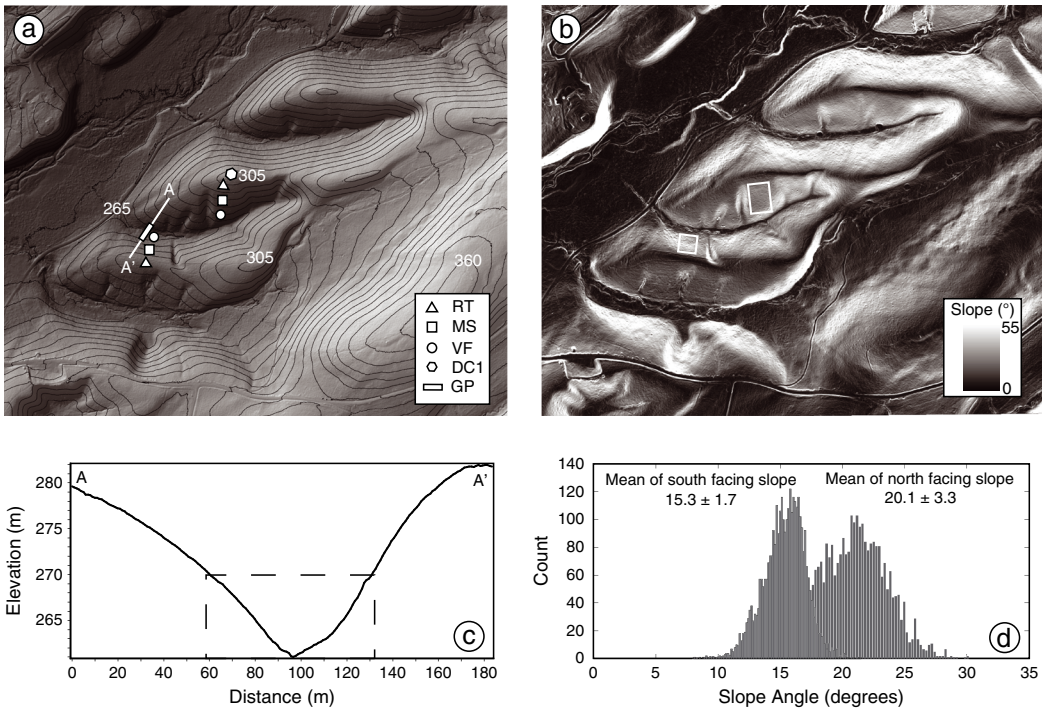

Figure 2. (a) Map view of the SSHO showing sample positions. White symbols indicate sample locations from hand augers (RT–ridgetop; MS–midslope; VF–valley floor), from a bedrock core (DC1), and from shallow subsurface cores along the valley floor (GP). The white line corresponds to the topographic profile presented in Figures 2c and 5. (b) Distribution of topographic gradient throughout the SSHO. Boxes show regions of relatively planar sections of the north and south hillslopes. (c) Topographic profile across the SSHO. The dashed box shows the area of Figure 5. (d) Histograms showing the distributions of hillslope gradients from regions in Figure 2b. These data suggest a dependence of mean hillslope gradients on aspect.

et al., 2010, 2013]. At SSHO, depletion of U-series isotopes was interpreted to reflect regolith production over 7–40 ka [*Ma et al*., 2010, 2013]. The shortest residence times were associated with ridgetop sites—11 and 9 ky for the north and south ridgetops, respectively. Regolith at midslope and valley floor positions exhibited significantly greater depletion, which *Ma et al*. [2010] interpreted as reflecting slower rates of regolith production beneath thicker soils.

2.2. Regolith Development and Transport Deduced From Meteoric ^{10}Be

[12] Early applications of cosmogenic isotopes relied on the delivery of ^{10}Be to landscapes in meteoric precipitation [*Lal and Peters*, 1967; *Monaghan et al*., 1983; *Pavich et al*, 1985; *McKean et al*., 1993]. Although this technique was supplanted for nearly a decade by the advent of techniques to measure extremely low concentrations associated with in situ production of ^{10}Be [*Bierman and Turner*, 1995; *Bierman and Steig*, 1996; *Heimsath et al*., 1997; *Heimsath et al*., 1999; *Riebe et al*., 2004], the application of meteoric ^{10}Be has been revived in recent years [*Jungers et al*., 2009; *Mackey et al*., 2009; *Willenbring and von Blanckenburg*, 2010a, 2010b; *West et al*., 2011; *Bacon et al*., 2012]. Inventories of meteoric ^{10}Be in stable or eroding regolith profiles provide an estimate of the duration of time over which ^{10}Be has accumulated, provided one can estimate the rate of ^{10}Be delivery [*Graly et al*., 2010a]. Recent efforts comparing short-term (months to years) delivery rate estimates with long-term (geologic) ^{10}Be accumulation rates [*Willenbring and von Blanckenburg*, 2010b; *Reusser and Bierman*, 2010; *Graly et al*., 2010a, 2010b] suggest that, in most climate regimes where delivery is primarily via rainfall, delivery rates for meteoric ^{10}Be are relatively constant over time.

[13] The concentration of meteoric ^{10}Be in regolith is controlled by several factors, including the delivery rate of meteoric ^{10}Be, the average residence time of surface materials (set by the erosion rate), and the intensity of pedogenic processes and the consequent subsurface mobility of meteoric ^{10}Be. Meteoric ^{10}Be is formed in the atmosphere as a product of spallation reactions between cosmic rays and ^{16}O and ^{14}N [*Lal and Peters*, 1967]. It quickly adheres to dust in the atmosphere and is then delivered to the Earth's surface via precipitation and dry fall. The delivery rate for meteoric ^{10}Be by precipitation is ~1.2–2.0 × 10^6 at cm^{-2} yr^{-1} for midlatitudes in the Northern Hemisphere [*Graly et al*., 2010a; *Reusser et al.*, 2010]. Empirically derived delivery rates for meteoric ^{10}Be consider mean annual precipitation; however, they do not include reworked ^{10}Be delivered by aeolian deposition, which can add substantial variability in actual ^{10}Be delivery from site to site [*Monaghan et al*., 1986].

[14] Meteorically delivered ^{10}Be is adsorbed to particle surfaces within the uppermost decimeters of regolith. The extent and distribution of ^{10}Be accumulation is controlled by regolith pH [*Pavich et al*., 1986; *You et al*., 1989; *Brown et al*., 1992; *Graly et al*., 2010b], mineralogy [*You et al*., 1989; *Aldahan et al*., 1999], and the rate of mass removal from the land surface by erosion [*Pavich et al*., 1985; *Graly et al*., 2010b]. If steady state regolith thickness is assumed, such that regolith erosion keeps pace with regolith production, the inventory of meteoric ^{10}Be in a regolith profile can be related to the erosion rate and, thus, a residence time [*Brown et al*., 1988].

[15] Residence times estimated using meteoric ^{10}Be for hillslopes in the eastern United States range from as long as ~1 My for regolith in the Piedmont province of Virginia and South Carolina [*Pavich et al*., 1985; *Bacon et al*., 2012] to as short as ~21 ky for regolith forming on steep hillslopes in the Great Smoky Mountains, NC [*Jungers et al*., 2009]. One important caveat is that removal of regolith, possibly associated with land use changes during early colonization of the eastern United States [*Costa*, 1975; *Walter and Merritts*, 2008], will reduce the measured inventory of meteoric ^{10}Be [*Valette-Silver et al*., 1986; *Harden et al*., 2002; *Reusser and Bierman*, 2010]. In all cases, residence time estimates using meteoric ^{10}Be are considered minima, as the amount of surface erosion is typically not known a priori.

2.3. Dependence of Regolith Transport on Hillslope Gradient

[16] Since the recognition that hillslope gradients adjust to the mass balance of regolith flux downslope [*Davis*, 1892; *Gilbert*, 1909], workers have sought to understand the quantitative relationship between the rates of regolith production, transport, and hillslope topography [*Culling*, 1963; *Kirkby*, 1971]. For much of the last century, it has been hypothesized that the downslope flux of regolith is linearly proportional to the local hillslope gradient

$$q = -K_1 \frac{\partial z}{\partial x} \tag{1}$$

where K_1 is a proportionality constant ($L^2\,t^{-1}$), analogous to a diffusion coefficient [*Culling*, 1963]. The "diffusive" behavior described by equation (1) is typically attributed to dilatational processes such as freeze-thaw, root growth and decay, and wetting and drying cycles [e.g., *Dietrich et al*., 2003]. This relationship has been of great utility in landscape modeling studies [e.g., *Tucker and Slingerland*, 1994; *Fernandes and Dietrich*, 1997], has been applied successfully to models of the degradation of fault scarps in noncohesive substrate [*Hanks et al*., 1984; *Pelletier et al*., 2006], and appears to explain much of the first-order structure of landscape topography [*Perron et al*., 2009; *Perron and Fagherazzi*, 2012]. Despite its appeal, few studies have been able to confirm quantitatively this rule with direct measures of regolith flux [*McKean et al*., 1993; *Small et al*., 1999]. Moreover, it is now well established that hillslopes in steep, often tectonically active landscapes exhibit profiles that are more consistent with a nonlinear relationship between hillslope gradient and regolith flux [*Roering et al*., 1999, 2001; *Gabet*, 2003; *Roering*, 2008]. Although the use of such models introduces a second free parameter, an empirically estimated "critical slope" angle at which regolith flux is infinite [*Roering et al*., 1999], it seems clear that the transport efficiency of bioturbation [*Gabet et al*., 2003], dry ravel [*Gabet*, 2003], and tree throw [*Roering et al*., 2010] on steep hillslopes changes with local topographic gradient.

[17] In recent years, workers have proposed that the downslope flux of regolith depends additionally on the depth of regolith; rules of this form typically consider transport

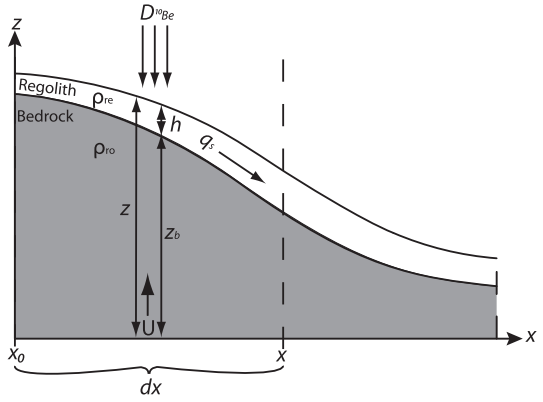

Figure 3. Definition sketch for the derivation of mass balance of regolith and meteoric ^{10}Be flux along a hillslope transect. $D^{10}Be$ is the delivery rate of meteoric ^{10}Be (at $cm^{-2}\ yr^{-1}$), ρ_{re} and ρ_{ro} are regolith and rock bulk densities, respectively ($g\,cm^{-3}$), z and z_b are the ground surface and bedrock surface elevations, respectively (cm), q is the lateral volumetric flux of regolith ($cm^2\ yr^{-1}$), and U is local uplift rate ($cm\ yr^{-1}$).

rates to depend on the product of local topographic gradient and regolith thickness [*Heimsath et al*., 2005; *Yoo et al*., 2007; *Roering*, 2008; *Pelletier et al*., 2011]:

$$q = -K_2 h \frac{\partial z}{\partial x} \tag{2}$$

here K_2 is a rate constant ($L\,t^{-1}$) and h is the regolith thickness (L). In this case, the regolith is defined as the mobile layer that is moving downslope. This formulation broadly encompasses the "diffusive mechanisms" associated with equation (1) (freeze-thaw, root growth and decay, bioturbation, wetting and drying cycles) but acknowledges the depth-dependent nature of the magnitude of disturbances associated with these mechanisms [*Heimsath et al*., 1997; *Gabet et al*., 2003; *Furbish et al*., 2009; *Roering et al*., 2010].

3. Derivation of Mass Balance of Meteoric ^{10}Be on Eroding Hillslopes

[18] Although meteoric ^{10}Be has previously been used as a tracer of regolith flux [*Monaghan et al*., 1992; *McKean et al*., 1993; *Jungers et al*., 2009], we present here a full derivation of the mass balance for an eroding hillslope. This discussion highlights necessary assumptions and simplifications that underlie the application to measure regolith flux. We calculate meteoric ^{10}Be inventories following *Brown et al*. [1988],

$$I_{\mathrm{Be}} = \int_{z_b}^{z} N \rho_{re} dz \tag{3}$$

where I_{Be} is the total inventory of ^{10}Be calculated for a given sample ($at\ cm^{-2}$), z is the elevation of the land surface (cm), z_b is the elevation of the bedrock-regolith interface (cm), N is the measured ^{10}Be concentration ($at\ g\ sample^{-1}$), ρ_{re} is the depth-averaged regolith density of the sample ($g\,cm^{-3}$), and dz is the sample depth interval (cm). For the total inventory to be calculated, the total sampling depth must extend to the base of the regolith (here defined as the mobile regolith layer) or to the furthest penetration of meteoric ^{10}Be. Assuming the delivery rate of meteoric ^{10}Be has been constant over the recent geologic past and the inventory of ^{10}Be in regolith is at a steady state between delivery and removal, a minimum regolith residence time can be calculated using the equation

$$t = \left(\frac{-1}{\lambda}\right) \ln\left(1 - \frac{\lambda I_{\mathrm{Be}}}{D}\right) \tag{4}$$

where t is time in years, λ is the radioactive decay constant for ^{10}Be, equal to $5.1 \times 10^{-7}\ year^{-1}$ [*Nishiizumi et al*., 2007], and D ($at\ cm^{-2}\ yr^{-1}$) is the delivery rate. This relationship is limited to settings such as ridgetops where no net ^{10}Be accumulation results from regolith transport. Likewise, regolith erosion rates can be estimated along ridgetops assuming steady state (i.e., where regolith erosion is balanced by regolith production) using measured meteoric ^{10}Be inventories

$$E = \frac{(D - \lambda I_{\mathrm{Be}})}{C_m} \tag{5}$$

where E is the erosion rate ($cm\ yr^{-1}$) and C_m is the ^{10}Be concentration in the uppermost surface sample ($at\ cm^{-3}$), inferred to be the eroding material [*Brown et al*., 1988].

[19] One can calculate volumetric flux rates of regolith, the weathered material available to move downslope by gravity-driven processes, along a hillslope by invoking the conservation of mass of both mobile regolith and adsorbed meteoric ^{10}Be in two dimensions (Figure 3). We begin this derivation with a statement of conservation of mass of regolith and bedrock in a Cartesian reference frame (Figure 3). Definitions of relevant variables are given in Table 1.

[20] Conservation of mass of regolith and bedrock dictates that the time rate of change of mass in the control volume is

$$\frac{\partial(\rho_{ro} z_b + \rho_{re} h)}{\partial t} 1 \mathrm{d}x = \rho_{re} q 1 - \left[\rho_{re} q 1 + \frac{\partial \rho_{re} q 1}{\partial x} \mathrm{d}x\right] + \rho_{ro} U 1 \mathrm{d}x \tag{6}$$

where ρ_{ro} is the bedrock density ($g\,cm^{-3}$), ρ_{re} is the depth-averaged regolith density ($g\,cm^{-3}$), h is the regolith thickness

Table 1. Variable Definitions for Equations (6)–(30)

Variable	Definition
Cre(x,t)	Concentration of ^{10}Be atoms in regolith in units of mass of ^{10}Be per unit mass of regolith (dimensionless)
Cre(*x*,*t*)	Concentration of ^{10}Be atoms in bedrock in units of mass of ^{10}Be per unit mass of bedrock (dimensionless)
m_a	Mass of a ^{10}Be atom ($g\ at^{-1}$)
D(*t*)	Atmospheric ^{10}Be delivery rate to the ground surface ($at\ cm^{-2}\ yr^{-1}$)
V=*q*/*h*	*x*-directed, depth-averaged regolith velocity (volumetric regolith flux per unit width divided by regolith thickness, $cm\ yr^{-1}$)
z_b	Elevation of bedrock-regolith interface (cm)
z	Elevation of ground surface (cm)
h	$z_b - z$ (cm)
ρ_{re}	Bulk density of regolith ($g\ cm^{-3}$)
ρ_{ro}	Bulk density of bedrock ($g\ cm^{-3}$)
λ	Radioactive decay constant ($5.1 \times 10^{-7}\ yr^{-1}$)
W	Bedrock weathering rate ($cm\ yr^{-1}$)
U	Uplift rate ($cm\ yr^{-1}$)

(cm), q is the flux of regolith down the hillslope (cm^2 yr^{-1}), equal to the product of h and the depth-averaged creep velocity (V, cm yr^{-1}), and U is the uplift rate (cm yr^{-1}). Here the left-hand side (LHS) represents the time rate of change of bedrock and regolith mass, and the terms on the right-hand side (RHS) represent the flux of regolith into the control volume, the regolith flux out of the control volume (by Taylor series expansion), and the upward flux of bedrock mass into the control volume. The unit value (1) is merely a place holder to explicitly denote unit width. Assuming spatial and temporal constancy of ρ_{re} and ρ_{ro}, the equation can be simplified to

$$\rho_{ro}\frac{\partial z_b}{\partial t}+\rho_{re}\frac{\partial h}{\partial t}=-\rho_{re}\frac{\partial q}{\partial x}+\rho_{ro}U \tag{7}$$

[21] By definition, $h=z-z_b$ and expanding the second term on the LHS produces

$$\rho_{ro}\frac{\partial z_b}{\partial t}+\rho_{re}\frac{\partial z}{\partial t}-\rho_{re}\frac{\partial z_b}{\partial t}=-\rho_{re}\frac{\partial q}{\partial x}+\rho_{ro}U \tag{8}$$

[22] Dividing through by ρ_{re} produces

$$\frac{\rho_{ro}}{\rho_{re}}\frac{\partial z_b}{\partial t}+\frac{\partial z}{\partial t}-\frac{\partial z_b}{\partial t}=-\frac{\partial q}{\partial x}+\frac{\rho_{ro}}{\rho_{re}}U \tag{9}$$

[23] Combining terms produces an expression for conservation of regolith mass on a hillslope

$$\frac{\partial z}{\partial t}-\left[1-\frac{\rho_{ro}}{\rho_{re}}\right]\frac{\partial z_b}{\partial t}+\frac{\partial q}{\partial x}-\frac{\rho_{ro}}{\rho_{re}}U=0 \tag{10}$$

[24] Incorporating a second conservation of mass, that of meteoric ^{10}Be on a hillslope, allows us to write

$$\begin{aligned}\frac{\partial(\rho_{re}C_{re}h+\rho_{ro}C_{ro}z_b)}{\partial t}1\mathrm{d}x=&-\rho_{re}\frac{\partial C_{re}q}{\partial x}1\mathrm{d}x+Dm_a1\mathrm{d}x\\&+\rho_{ro}C_{ro}U1\mathrm{d}x-\rho_{re}\lambda C_{re}h1\mathrm{d}x\\&-\rho_{ro}\lambda C_{ro}z_b1\mathrm{d}x\end{aligned} \tag{11}$$

where C_{ro} and C_{re} are the dimensionless concentrations of meteoric ^{10}Be in the bedrock and regolith and m_a is the atomic mass of ^{10}Be (kg atom^{-1}). Equation (11) can be simplified by assuming that ρ_{re} and ρ_{ro} are temporally and spatially constant, dividing through by 1dx and using the product rule on the derivatives to yield

$$\begin{aligned}&\frac{\rho_{re}h\partial C_{re}}{\partial t}+\frac{\rho_{re}C_{re}\partial h}{\partial t}+\frac{\rho_{ro}z_b\partial C_{ro}}{\partial t}+\frac{\rho_{ro}C_{ro}\partial z_b}{\partial t}=\\&-\rho_{re}\left[q\frac{\partial C_{re}}{\partial x}+C_{re}\frac{\partial q}{\partial x}\right]+Dm_a+\rho_{ro}C_{ro}U\\&-\rho_{re}\lambda C_{re}h-\rho_{ro}\lambda C_{ro}z_b\end{aligned} \tag{12}$$

[25] By definition, h is the difference between the elevation of the bedrock-regolith interface (z_b) and the surface elevation (defined here as z); therefore, the second term on the left-hand side (LHS) of equation (12) can be expanded, producing

$$\begin{aligned}&\frac{\rho_{re}h\partial C}{\partial t}+\frac{\rho_{re}C_{re}\partial z}{\partial t}-\frac{\rho_{re}C_{re}\partial z_b}{\partial t}+\frac{\rho_{ro}z_b\partial C_{ro}}{\partial t}+\frac{\rho_{ro}C_{ro}\partial z_b}{\partial t}=\\&-\rho_{re}\left[q\frac{\partial C_{re}}{\partial x}+C_{re}\frac{\partial q}{\partial x}\right]+Dm_a+\rho_{ro}C_{ro}U\\&-\rho_{re}C_{re}\lambda h-\rho_{ro}\lambda C_{ro}z_b\end{aligned} \tag{13}$$

[26] Dividing by $\rho_{re}C_{re}$ and grouping terms yield

$$\begin{aligned}&\frac{h}{C_{re}}\frac{\partial C_{re}}{\partial t}+\frac{\rho_{ro}z_b}{\rho_{re}C_{re}}\frac{\partial C_{ro}}{\partial t}-\frac{Dm_a}{\rho_{re}C_{re}}+\frac{q}{C_{re}}\frac{\partial C_{re}}{\partial x}+\lambda h+\frac{\rho_{ro}}{\rho_{re}}\lambda\frac{C_{ro}}{C_{re}}z_b\\&+\left[\frac{\rho_{ro}C_{ro}}{\rho_{re}C_{re}}-1\right]\frac{\partial z_b}{\partial t}+\frac{\partial z}{\partial t}+\frac{\partial q}{\partial x}-\frac{\rho_{ro}C_{ro}}{\rho_{re}C_{re}}U=0\end{aligned} \tag{14}$$

[27] The second line of equation (14) contains a statement of conservation of regolith mass that sums to zero and can be dropped, as the following steps illustrate. By conservation of bedrock mass, we know that

$$\frac{\partial z_b}{\partial t}=-W+U \tag{15}$$

and therefore the LHS of the second line of equation (14) expands to

$$\begin{aligned}&\frac{h}{C_{re}}\frac{\partial C_{re}}{\partial t}+\frac{\rho_{ro}z_b}{\rho_{re}C_{re}}\frac{\partial C_{ro}}{\partial t}-\frac{Dm_a}{\rho_{re}C_{re}}+\frac{q}{C_{re}}\frac{\partial C_{re}}{\partial x}+\lambda h+\frac{\rho_{ro}}{\rho_{re}}\lambda\frac{C_{ro}}{C_{re}}z_b\\&-\frac{\rho_{ro}C_{ro}}{\rho_{re}C_{re}}W-U+W+\frac{\rho_{ro}C_{ro}}{\rho_{re}C_{re}}U+\frac{\partial z}{\partial t}+\frac{\partial q}{\partial x}-\frac{\rho_{ro}C_{ro}}{\rho_{re}C_{re}}U=0\end{aligned} \tag{16}$$

or

$$\begin{aligned}&\frac{h}{C_{re}}\frac{\partial C_{re}}{\partial t}+\frac{\rho_{ro}z_b}{\rho_{re}C_{re}}\frac{\partial C_{ro}}{\partial t}-\frac{Dm_a}{\rho_{re}C_{re}}+\frac{q}{C_{re}}\frac{\partial C_{re}}{\partial x}+\lambda h+\frac{\rho_{ro}}{\rho_{re}}\lambda\frac{C_{ro}}{C_{re}}z_b\\&\frac{\partial z}{\partial t}-\left[\frac{\rho_{ro}C_{ro}}{\rho_{re}C_{re}}-1\right]W+\frac{\partial q}{\partial x}-U=0\end{aligned} \tag{17}$$

[28] By conservation of regolith mass (equation (10)), we know that

$$\frac{\partial z}{\partial t}-\left[\frac{\rho_{ro}}{\rho_{re}}-1\right]W+\frac{\partial q}{\partial x}-U=0 \tag{18}$$

[29] Notice that this differs from the second line of equation (17) by a factor of C_{ro}/C_{re}. Because the LHS of equation (18) sums to zero, we can subtract it from equation (17) to yield

$$\begin{aligned}&\frac{h}{C_{re}}\frac{\partial C_{re}}{\partial t}+\frac{\rho_{ro}z_b}{\rho_{re}C_{re}}\frac{\partial C_{ro}}{\partial t}-\frac{Dm_a}{\rho_{re}C_{re}}+\frac{q}{C_{re}}\frac{\partial C_{re}}{\partial x}+\lambda h\\&+\frac{\rho_{ro}}{\rho_{re}}\lambda\frac{C_{ro}}{C_{re}}z_b\frac{\partial z}{\partial t}-\left[\frac{\rho_{ro}C_{ro}}{\rho_{re}C_{re}}-1\right]W+\frac{\partial q}{\partial x}-U\\&-\left[\frac{\partial z}{\partial t}-\left[\frac{\rho_{ro}}{\rho_{re}}-1\right]W+\frac{\partial q}{\partial x}-U\right]=0\end{aligned} \tag{19}$$

or

$$\frac{h}{C_{re}}\frac{\partial C_{re}}{\partial t}+\frac{\rho_{ro}z_b}{\rho_{re}C_{re}}\frac{\partial C_{ro}}{\partial t}-\frac{Dm_a}{\rho_{re}C_{re}}+\frac{q}{C_{re}}\frac{\partial C_{re}}{\partial x}+\lambda h+\frac{\rho_{ro}}{\rho_{re}}\lambda\frac{C_{ro}}{C_{re}}z_b\frac{\rho_{ro}}{\rho_{re}}\left[\frac{C_{re}-C_{ro}}{C_{re}}\right]W=0 \quad (20)$$

[30] Thus, after multiplying through by C_{re}/h (here, essentially dividing through by h/C_{re}, terms introduced by the product rule expansion), equation (20) becomes

$$\frac{\partial C_{re}}{\partial t}+\frac{\rho_{ro}z_b}{\rho_{re}h}\frac{\partial C_{ro}}{\partial t}=\frac{Dm_a}{\rho_{re}h}-V\frac{\partial C_{re}}{\partial x}-\lambda C_{re}-\frac{\rho_{ro}}{\rho_{re}}\lambda\frac{C_{ro}}{h}z_b-\frac{\rho_{ro}}{\rho_{re}}\left[\frac{C_{re}-C_{ro}}{h}\right]W \quad (21)$$

[31] This is the full expression relating meteoric ^{10}Be concentration, creep velocity, regolith thickness, and regolith production.

[32] An analysis of the orders of magnitude of each term in equation (21) reveals that the sink terms associated with radioactive ^{10}Be decay (third and fourth terms on RHS) are approximately five orders of magnitude less than the meteoric ^{10}Be source term and can thus be ignored. Previous workers have also made this assumption in both meteoric [*Monaghan et al*., 1992; *McKean et al*., 1993] and in situ applications [*Bierman and Steig*, 1996; *Granger*, 2006; *Gosse and Phillips*, 2001]. Similarly, assuming that all meteorically delivered ^{10}Be is scavenged by the mobile regolith and does not penetrate to underlying saprolite or rock, C_{ro} can be considered negligible, allowing us to simplify equation (21) to

$$\frac{\partial C_{re}}{\partial t}+V\frac{\partial C_{re}}{\partial x}=\frac{Dm_a}{h\rho_{re}}-\frac{\rho_{ro}}{\rho_{re}}\frac{C_{re}}{h}W \quad (22)$$

[33] Furthermore, in regions of the landscape where the time rate of change of meteoric ^{10}Be concentration in regolith has reached zero, i.e., where the rate of addition from rainfall, dilution from the conversion of bedrock to fresh regolith, and transport downslope sum to zero, equation (22) reduces to

$$\frac{\mathrm{d}C_{re}}{\mathrm{d}x}=\frac{Dm_a}{Vh\rho_{re}}-\frac{\rho_{ro}}{\rho_{re}}\frac{C_{re}}{Vh}W \quad (23)$$

[34] Here another order of magnitude analysis reveals that the second term on the RHS, representing the rate of bedrock conversion to regolith, is approximately five orders of magnitude less than the rate of meteoric ^{10}Be delivery and thus can be ignored to obtain

$$Vh\frac{\mathrm{d}C_{re}}{\mathrm{d}x}=\frac{Dm_a}{\rho_{re}} \quad (24)$$

[35] Finally, knowing that volumetric flux per unit width (q) is, by definition, the product of regolith thickness and depth-averaged velocity (h and V, respectively), one can integrate equation (24) from x_0 to x, where x_0 designates the position of the ridge crest, to yield

$$C_{re}q\big|_{(C_{re}q)_0}^{C_{re}q}=\frac{Dm_a}{\rho_{re}}(x-x_0) \quad (25)$$

[36] This result is similar to the formulation presented by *Monaghan et al*. [1992] and *McKean et al*. [1993], but we retain the full derivation here to emphasize the necessary assumptions. Evaluating equation (25) allows an expression for regolith flux,

$$q=\frac{Dm_a}{C_{re}\rho_{re}}(x-x_0) \quad (26)$$

where $(x-x_0)$ formally represents the length scale over which a given average C_{re} and ρ_{re} can be used to estimate locally uniform mobile regolith flux, q (i.e., over some infinitesimally small interval, dx). We note that in situ ^{10}Be traveling in regolith grains is ignored in this treatment, as its contribution to the total ^{10}Be mass flux is over five orders of magnitude less than that of meteoric ^{10}Be.

[37] Rearranging equation (26) allows us to solve for depth-averaged creep velocities,

$$qC_{re}\rho_{re}=Dm_a(x-x_0) \quad (27)$$

[38] Knowing that $q=Vh$, equation (27) becomes

$$VhC_{re}\rho_{re}=Dm_a(x-x_0) \quad (28)$$

[39] From equation (3), we know that

$$hC_{re}\rho_{re}=I_{Be} \quad (29)$$

[40] Thus, the velocity at any position x downslope can be calculated as

$$V=\frac{Dm_a(x-x_0)}{I_{Be}} \quad (30)$$

[41] Equation (30) is similar to the formulation presented by *Jungers et al*. [2009] but remains consistent with our definition of the control volume and mass balance.

4. Methods

4.1. Sampling and Analysis for Meteoric ^{10}Be

[42] We measured meteoric ^{10}Be depth profiles using 44 samples of bulk regolith from two ridge-to-valley transects along the northern ($n=28$) and southern ($n=16$) hillslopes of the SSHO watershed (Figure 2a). Profile samples were collected at three locations along the transects, representing the north and south planar ridge top (NP-, SPRT), middle slope (NP-, SPMS), and toe slope or valley floor positions (NP-, SPVF). These hillslopes are characterized by nonconvergent sediment flow and thus have been termed "planar" in previous studies to distinguish them from swales with greater topographic curvature [*Jin et al*., 2010; *Ma et al*., 2010]. The profile sample sites are coincident with

samples from both *Jin et al*. [2010] and *Ma et al*. [2010; 2013] and were collected at ~10 cm depth intervals using a 2 in. soil auger until refusal. Samples were homogenized over each depth interval. For the purposes of this work, we consider hand auger refusal to represent the depth of mobile regolith. Field observations of regolith cross sections observed in excavated trenches support the interpretation that the entire augerable thickness is mobile (A. Dere, personal communication, 2010). We will refer to hand-augerable material as mobile regolith throughout the remainder of this paper.

[43] Twenty-nine additional bulk mobile regolith samples were collected and analyzed to assess the variability of ^{10}Be across each hillslope. Sample locations formed a grid-like pattern across each hillslope (Figure 4). Single, depth-averaged (from mineral-soil surface to base of mobile regolith) samples were taken at ridge top, midslope, and valley floor sample sites, and the homogenized samples were used for meteoric ^{10}Be measurements. Samples collected between the ridge top, midslope, and valley floor positions (labeled upper slope US and lower slope LS—Figure 4 and Table 6) were mixed before analysis, and a single, amalgamated meteoric ^{10}Be measurement was taken to represent the average ^{10}Be concentration at that position. Bulk regolith density (ρ_{re}) was calculated for each sample as a depth-averaged density, using depth-dependent regolith bulk densities measured by *Jin et al*. [2010].

[44] To test the assumption that ^{10}Be is retained in mobile regolith and is not transported to depth below the regolith-bedrock boundary, we analyzed samples from a deep (24 m) core drilled into the north ridge ($n = 14$, Figure 2a). Bedrock samples were collected using an air-rotary drill, collecting chips at 10–20 cm intervals [*Jin et al*., 2010]. Samples were homogenized from individual depth ranges before analysis. Because we cannot preclude mixing of chips from varying depths during drilling, our samples may represent mixing beyond the 10–20 cm depth interval. Nonetheless, these data provide a first-order evaluation of the mobility of meteoric ^{10}Be in the SSHO substrate.

[45] Samples, including several process blanks, were prepared in batches of 16 in the University of Vermont cosmogenic nuclide extraction laboratory following a modification of the flux fusion method presented by *Stone* [1998]. Approximately 0.5 g of finely milled material was mixed with KHF and $NaSO_4$ along with ~300 μg of ^{9}Be-carrier (SPEX brand). The mixture was fused over a natural gas/O_2 flame in a Pt crucible for several minutes until the resulting melt was clear. After cooling, the crucible containing the solidified fusion cake was plunged into a Teflon beaker containing Milli-Q (18.2 Mohm) water where it remained for a 24 h leaching period. Excess K in the leachate was removed by $HClO_3$ precipitation, and the remaining Be was precipitated as a hydroxide. The hydroxide was burned to BeO, mixed with an equimolar amount of Nb metal powder, and loaded into stainless steel cathodes for ^{10}Be/^{9}Be ratio measurements by accelerator mass spectrometry (AMS) at the Center for Accelerator Mass Spectrometry, Lawrence Livermore National Laboratory.

[46] Beryllium isotopic ratios were measured in multiple data acquisitions of each target using post accelerator stripping to reduce ^{10}B isobaric interference. Analyses of each target were repeated between 2 and 4 times. Three secondary standards were run repeatedly to verify linearity of the isotopic analyses over a range of ratios. Results were normalized to the 07KNSTD series of standards, using a primary standard with a reported ^{10}Be/^{9}Be ratio of 2.85×10^{-12} [*Nishiizumi et al*., 2007]. Standard-corrected isotopic ratios ranged widely from 2.79×10^{-14} to 1.99×10^{-11}. We made a blank correction by subtracting the average of the process blanks run with two batches of samples ($n = 2$, $\sigma = 2.3 \pm 1.1 \times 10^{-14}$) from each sample ratio. Because most of these samples contained so much ^{10}Be and the average ratio was high, the resulting blank correction is inconsequential except for the deepest core samples.

4.2. Sampling and Analysis of Stratigraphic Cores

[47] To explore the character and thickness of deposits in the valley floor, we collected 15 shallow subsurface cores, using a Geoprobe 6620 direct push corer. Hollow, 5 cm diameter sample rods lined with acetate sleeves were hammered vertically through the regolith until refusal, the depth of competent bedrock. Samples were collected and stored in the acetate sleeves until preparation for analysis. A 2.5 cm wide cut was taken from the length of the sleeve before analysis to allow for direct observation of the regolith layer without disturbing the intact core. The cores were collected perpendicular to the channel across the valley floor just downstream of the south hillslope transect (Figure 2a).

[48] Core spacing was approximately 3 m and spanned the subtle fill terrace present at the valley floor (Figures 2a and 2c). Our motivation for the core collection across the valley floor was to determine the nature and provenance of valley fill material that comprises the low terrace surface (Figure 1). Major changes in sediment characteristics with depth were recorded and included rock/grain type, grain size, grain sorting, grain packing, Munsell color, relative moisture content, and the amount of organic material present. Fence-type diagrams were then constructed using the logged core data to develop an understanding of the unconsolidated subsurface of the valley floor at SSHO. Two pieces of charcoal debris found in the core were collected using a steel trowel and stored in aluminum foil. The charcoal was analyzed at Beta Analytic, Inc. for ^{14}C content. The samples were pretreated sequentially with acid, alkali, and acid prior to combustion and analysis using accelerator mass spectrometry. ^{14}C ages were calibrated using INTCAL04 [*Reimer et al*., 2004].

5. Results

[49] The hillslopes at SSHO examined in this study are characterized by broad, convex ridge tops, relatively planar midsections, and concave toe slopes (Figure 5). As noted above, the hillslopes along the southern side of the catchment have higher gradients ($20.1° \pm 3.3°$) than northern slopes ($15.3° \pm 1.7°$). This shape is characteristic of our specific sample localities; throughout its midsection, the southern slope exhibits mean gradients of ~20°, whereas the northern slope averages ~15° (Figure 5). Topographic profiles extracted from the LiDAR digital elevation model reveal that the northern hillslope exhibits a pronounced planar midsection, but the southern hillslope is more convex-concave (Figure 5).

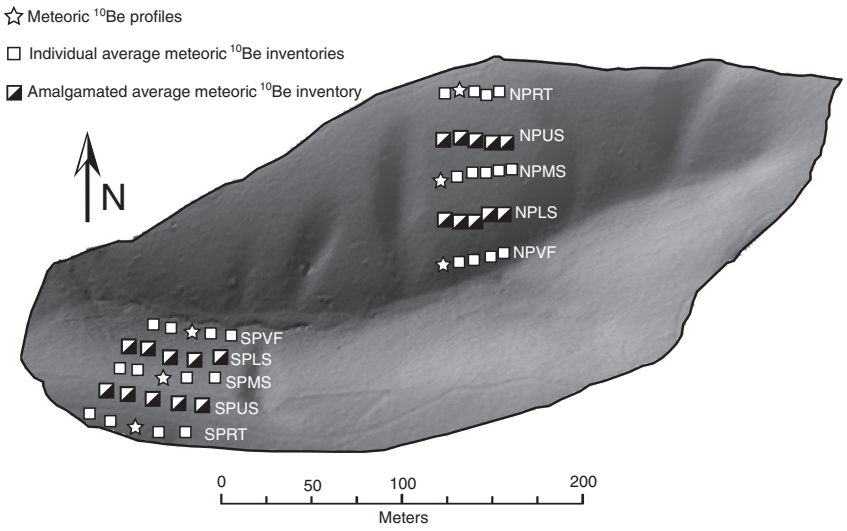

Figure 4. Detailed sampling and analysis strategy for the north and south hillslopes at SSHO. White stars indicate locations of meteoric ^{10}Be concentration depth profiles. White squares indicate locations at which we measured a single depth-averaged meteoric ^{10}Be concentration. Partially filled squares indicate sample positions where samples were amalgamated along contour lines to yield a single average measure of meteoric ^{10}Be concentration.

[50] Observations of mobile regolith depth in hand-augered sample sites reveal that mobile regolith on the ridgetops is relatively thin and thickens downslope on both sides of the catchment (Figures 5a and 5b). On the northern hillslope, mobile regolith thickens slightly downslope from 28 ± 8 cm ($n = 5$) at the ridge top to 39 ± 9 cm ($n = 5$) near the base of the transect. At the valley floor, the augerable thickness is 101 ± 15 cm ($n = 5$, Figures 5a and 5b). In

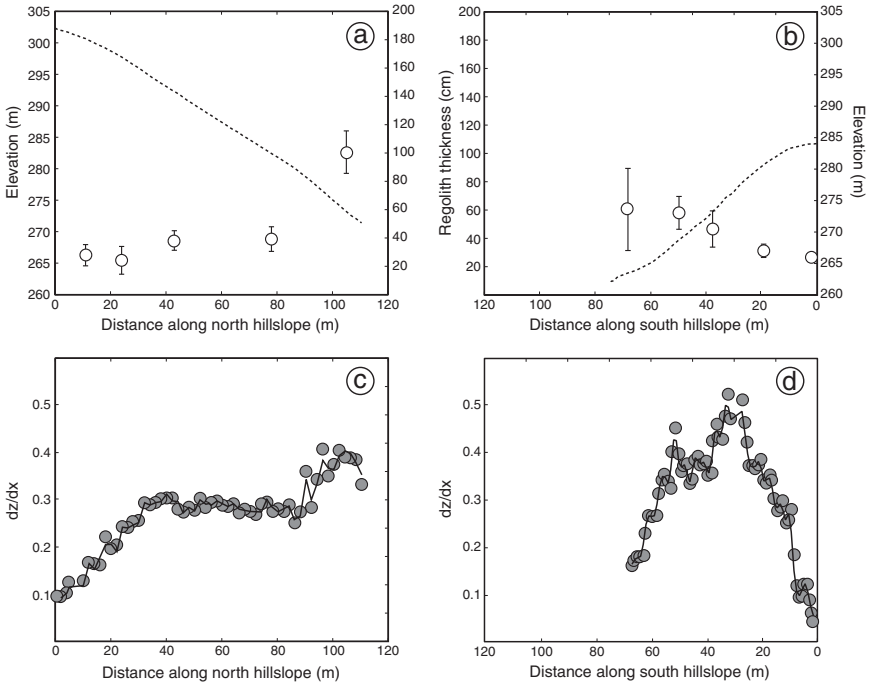

Figure 5. Topographic profiles along the (a) north and (b) south sample transects (dashed lines). *X* axes are flipped in Figures 5b and 5d to reflect the landscape profile if viewing from the mouth of the watershed. Note that these transects are traced along the ^{10}Be profile transects on the north and south hillslopes, not the transect shown in Figure 2c. Data show average depth of refusal for regolith on the north and south hillslopes at SSHO (Figures 5a and 5b). Error bars indicate 1 standard deviation from the mean at each hillslope position. Local topographic gradient along the (a) north and (b) south hillslope transects. Gradients are generally higher along the south hillslope than the north hillslope. The dark line represents a moving average [of 3 pixels] of individual pixel-to-pixel gradients.

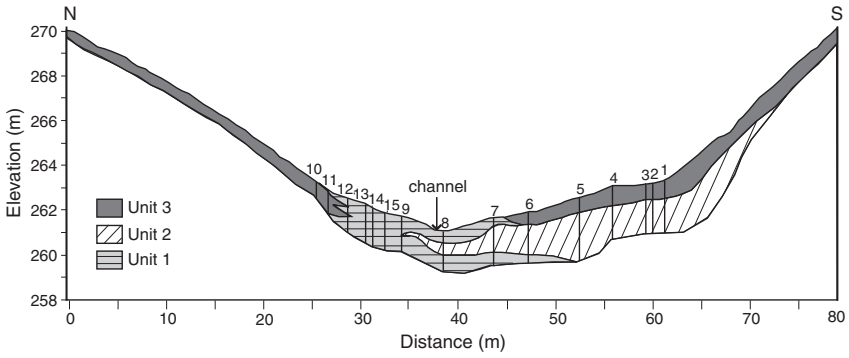

Figure 6. Composite cross section of valley floor stratigraphy inferred from shallow coring. The cross section only represents the lower portions of the SSHO catchment as shown in Figure 2c and does not represent the entire landscape topographic profile. Lithostratigraphic units are derived from core logs and are divided into three categories. Unit 1 represents alluvial deposits immediately adjacent to the present-day channel. Unit 2 represents poorly stratified colluvial material, interbedded with layers of more well-sorted sands and silts. Unit 3 represents massive, unstratified soil and mobile regolith on upland hillslopes.

contrast, mobile regolith thickness on the southern hillslope increases somewhat systematically from 27 ± 4 cm (n = 5) at the ridge top to 60 ± 29 cm (n = 5) at the valley floor position. Not only does the mean thickness increase downslope but so does the spatial variability in thickness across the hillslope (standard deviation of regolith thickness at the SPRT location—σ_{SPRT} = 15%, standard deviation of regolith thickness at the SPVF location—σ_{SPVF} = 48%). This pattern is not as pronounced on the northern hillslope (σ_{NPRT} = 15%, σ_{NPVF} = 27%).

5.1. Valley Floor Stratigraphy

[51] Although mobile regolith on upland hillslopes is relatively thin, subsurface cores collected across the valley floor of SSHO reveal that coarse alluvial and colluvial sediments extend to several meters depth beneath the axis of the valley (Figure 6). All cores were collected until refusal, and relatively fresh, competent bedrock was observed at the base of the cores. Fractures and/or bedding planes are present in this bedrock but are generally closed with little to no open pore space. Open fractures in fresh rock were observed at the base of only a few cores located south of the present-day channel. In general, deposits above this bedrock are poorly sorted with grain sizes ranging from silt to coarse gravel. Depth to bedrock along the transect ranged from 70 cm to ~3 m (Figure 6). Deposits are thickest near the valley floor but are somewhat asymmetric relative to the modern channel, extending ~10–15 m south of the channel (Figure 6).

[52] Near the axis of the valley, sediments are characterized by moderately well-sorted layers of medium to coarse sand interbedded with finer-grained layers of silt. Grains are generally comprised of shale chips and are crudely subhorizontally stratified. We refer to this facies association as Unit 1. Sandy layers are discontinuous between adjacent cores and are inferred to be lens-shaped in cross section. In general, Unit 1 fines upward, with coarse sand layers more frequently observed at depths greater than 50 cm. The sandy layers of Unit 1 are oxic as evidenced by a reddish color. The silty layers exhibited mottled coloring, with a mixture of oxic red and anoxic gray material. Unit 1 ranges in thickness from 51 to 126 cm, and interfingers with Units 2 and 3, described below.

[53] South of the axis of the valley, the subsurface stratigraphy is comprised primarily of interbedded layers of large, poorly sorted, unoriented subangular shale gravels with layers of better-sorted coarse sands and silts. We refer to this association as Unit 2, and we only observed it to the south and at depth under the modern channel. Unit 2 thins to the north, toward the valley axis, from ~160 to ~20 cm. The poorly sorted layers of unoriented rock fragments are generally thicker (~40 cm) than the better-sorted layers of sands and silts (~15 cm). All layers in Unit 2 contain considerable oxidized iron, inferred from their reddish color. Our description of Unit 2 is consistent with observations from excavated soil trenches (A. Dere, personal communication, 2010), namely, that a poorly sorted colluvial layer underlies regolith low on the southern hillslope that is not present on the northern hillslope.

[54] On hillslopes above the valley floor, we observed a relatively thin (~30–100 cm, Figures 5a and 5b) mantle of moderately to poorly sorted, structureless mobile regolith that directly overlies competent, relatively fresh bedrock above the valley floor. This unit (Unit 3) interfingers with Unit 1 in the subsurface immediately adjacent to the channel.

Table 2. Radiocarbon Ages Measured From Valley Fill Charcoal[a]

Sample ID	Measured Age	$^{13}C/^{12}C$	Conventional Age	2 Sigma Calibration
GP-04	840+/−40 BP	−26.9‰	810+/−40 BP	Cal A.D. 1160 to 1280 (Cal BP 790 to 670)
GP-05	1030+/−30 BP	−25.3‰	1030+/−30 BP	Cal A.D. 980 to 1030 (Cal BP 970 to 920)

[a]Ages calibrated using INTCAL04 (2004).

South of the channel, Unit 3 overlies Unit 2 and also interfingers with Unit 1 adjacent to the channel.

[55] The moderately well-sorted nature of Unit 1 is consistent with alluvial deposition along the paleochannel axis. In contrast, the unsorted and disoriented nature of Unit 2 appears to be more consistent with deposition from hillslope and colluvial processes. The structure of Unit 2 is qualitatively similar to the relict periglacial deposits described by *Clark and Ciolkosz* [1988], commonly found in the Valley and Ridge province of central Pennsylvania. Unit 3 appears to represent a mantle of mobile regolith developing atop in situ bedrock on the upper slopes of the watershed that is being transported and deposited above older stratigraphic units in the valley floor (Figure 6) and is thus equivalent to the augerable regolith that has been discussed previously [*Jin et al*., 2010; *Ma et al*., 2010].

[56] Our stratigraphic divisions of valley fill material are generally consistent with pedologic descriptions of the Ernest soil formation [*Lin et al*., 2006] with deep alternating layers of sandy loam and poorly sorted layers of coarse rock fragments and clay at depths greater than 50 cm. Our observations of the two northernmost cores (GP-10 and GP-11) are more consistent with pedologic descriptions of the Weikert and Berks series, which are shallower units that exhibit a general fining upward trend [*Lin et al*., 2006].

[57] Two charcoal samples were collected within Unit 3 south of the present-day channel within cores GP-04 and GP-05. These samples appeared to be charred woody debris, occurring as single pieces, each one approximately 1 cm in diameter. Radiocarbon dating of these samples yielded ages of 810 ± 40 and 1030 ± 30, respectively. Calibration of these ages to calendar years yields dates of 1160–1280 A.D. and 980–1030 A.D. (Table 2). Although this material is detrital charcoal and may be reworked, the consistency of both ages at the same stratigraphic depth imply that the upper 30–40 cm of Unit 3 in the valley floor has accumulated over the last ~1000 years.

[58] The depth of the base of Unit 3 inferred from our stratigraphic analysis is very near the depth of refusal for hand augering, and thus nearly all of the samples that we collected for ^{10}Be analysis correspond to Unit 3. However, Unit 2 appears to extend across the south side of the valley floor, and the depth of our samples from the SPVF site overlaps with the presence of this unit in our cores. Thus, we consider it likely that the deepest samples analyzed for ^{10}Be from the SPVF site represent material at the transition between Units 2 and 3.

5.2. Meteoric ^{10}Be Distribution in Bedrock

[59] The 14 samples analyzed from the deep core (DC1, Figure 2) contain relatively low concentrations of meteoric ^{10}Be, suggesting that only limited amounts of this isotope penetrate to bedrock beneath the mobile regolith at SSHO. Meteoric ^{10}Be concentrations in bedrock samples decline sharply with depth, decreasing by an order of magnitude from 1.7×10^8 at g^{-1} in the 0–18 cm interval to 5.0×10^7 at g^{-1} in the 18–30 cm interval (Figure 7a and Table 2). Concentrations remain low throughout the length of the bedrock core, ranging from 7.2×10^7 at g^{-1} to $< 1.3 \times 10^6$ at g^{-1}. At depths of 30–49, 150–170, and 1070–1090 cm, ^{10}Be concentrations are slightly elevated relative to neighboring samples (Figure 7a) but are still on the order of 10^7 at g^{-1}. Although these locally elevated concentrations could reflect some transport of meteoric ^{10}Be along fracture networks in the subsurface, it is also likely that these may reflect contamination by material falling from higher intervals into the borehole.

[60] The original regolith at the drill pad site was significantly modified during (and perhaps before) drilling, which prevents a direct comparison of bedrock ^{10}Be concentrations with those in overlying regolith. The drill site is adjacent to an access road that has been used over the past several decades for forest management activities. Thus, the uppermost samples from DC1 are not considered representative of undisturbed ridge top regolith, but rather reflect some mixture of mobile regolith and bedrock. Below, we compare inventories of meteoric ^{10}Be in the uppermost bedrock samples to evaluate the degree to which ^{10}Be is sequestered in the mobile regolith.

5.3. Meteoric ^{10}Be in Hillslope Regolith

[61] Meteoric ^{10}Be concentrations in mobile SSHO regolith are, on average, an order of magnitude higher than those measured at the top of the bedrock core and up to two orders of magnitude greater than concentrations at the base of the deep core (Figures 7c and 7d). At all 6 profile sample locations along the north and south hillslope transects, meteoric ^{10}Be concentrations decrease with depth (Figures 7c and 7d). At the northern ridge top site, meteoric ^{10}Be concentrations decrease from 7.49×10^8 at g^{-1} at the surface to 1.28×10^8 at g^{-1} at the base of mobile regolith (39 cm, Table 3). At the midslope position, meteoric ^{10}Be concentrations decrease from 1.03×10^9 at g^{-1} at the surface to 2.41×10^8 at g^{-1} at 40 cm. The concentration profile of meteoric ^{10}Be at the midslope position resembles an exponential decrease with depth. At the valley floor site, meteoric ^{10}Be concentrations decrease from 5.7×10^8 at g^{-1} to 1.43×10^8 at g^{-1} at depth (118 cm).

[62] Meteoric ^{10}Be concentration profiles measured on the southern hillslope closely resemble those measured on the northern hillslope. At the southern ridge top site, meteoric ^{10}Be concentrations decrease from 6.6×10^8 at g^{-1} at the surface to 2.6×10^8 at g^{-1} at 30 cm (Table 4). ^{10}Be concentrations at the midslope site decrease from 9.6×10^8 at g^{-1} at the surface to 2.3×10^8 at g^{-1} at 60 cm. Similar to the NPMS site, the profile at SPMS also appears exponential. At the valley floor site, although concentrations decreased with depth from 5.5×10^8 at g^{-1} at the surface to 2.7×10^8 at g^{-1} by 67 cm, the profile does not appear exponential (Figures 7c and 7d).

[63] We calculated the inventories of meteoric ^{10}Be for each of the 35 sample locations on the north ($n = 18$) and south ($n = 17$) hillslopes of SSHO, using equation (3). As indicated above, single, depth-averaged regolith bulk densities were used for each sample position for samples that were homogenized. Depth-specific regolith bulk densities were used for profile samples. Inventories at the ridge top, midslope, and valley floor positions were then averaged to represent the inventory at each hillslope position, for comparison to inventories measured for the amalgamated samples collected in between (US and LS, Figure 4). On both hillslopes, mean inventories increase systematically downslope, with the exception of the SPVF position (Figure 8 and Table 5). At the northern ridge top, the average meteoric ^{10}Be inventory is $1.89 \pm 0.55 \times 10^{10}$ at cm^{-2}.

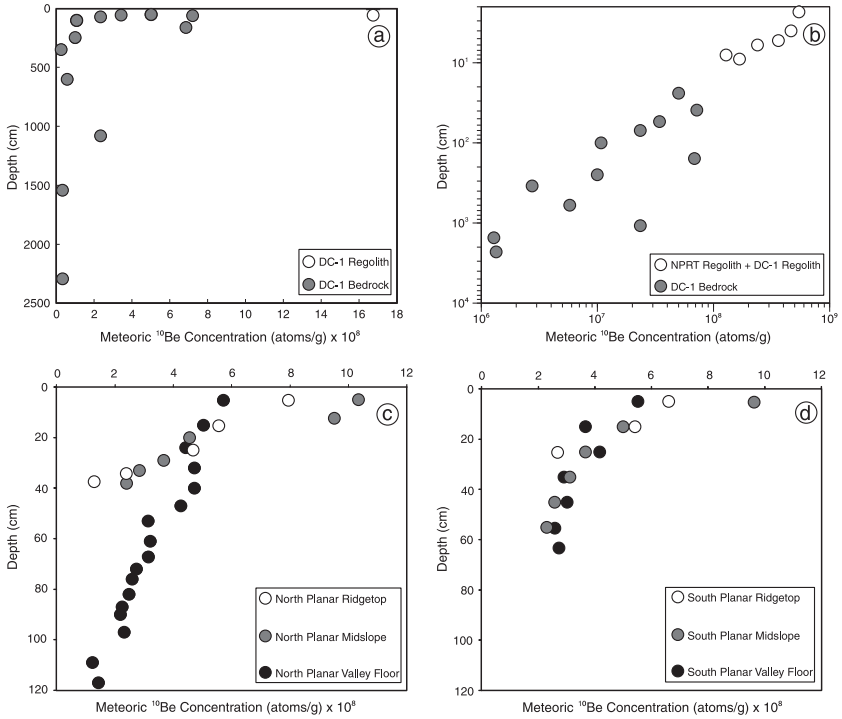

Figure 7. (a) Meteoric ^{10}Be concentration profile of the deep bedrock core (DC) drilled into the northern ridge. Open symbol represents uppermost sample from the DC1 location, interpreted to be regolith and not representative of bedrock ^{10}Be concentrations. Meteoric ^{10}Be concentrations decline sharply with depth within bedrock. (b) Comparison of meteoric ^{10}Be in core with concentrations at the adjacent north planar ridgetop regolith sample sites (NPRT–Figure 4). ^{10}Be concentrations are one to two orders of magnitude lower in bedrock than in regolith. The uppermost DC1 sample (open circle–Figure 7a) exhibits similar concentrations to the lowermost samples in the NPRT profile (open circle–Figure 7c) and is interpreted to reflect regolith atop the disturbed drill pad. (c) Meteoric ^{10}Be concentration profiles measured along the north hillslope transect. (d) Meteoric ^{10}Be concentration profiles measured along the south hillslope transect. All meteoric ^{10}Be profiles are consistent with addition at the surface and attenuation in regolith materials.

The uncertainties reported here are propagated from one standard deviation of the mean (1σ) mobile regolith depth for the five ridge top sites, and 1σ (~1–2%) uncertainty from the AMS measurements. The inventory immediately downslope of the northern ridge top is $1.68 \pm 0.42 \times 10^{10}$ at cm^{-2}, and increases at the midslope position to $2.54 \pm 0.62 \times 10^{10}$ at cm^{-2}, the lower slope position ($2.92 \pm 0.73 \times 10^{10}$ at cm^{-2}), and the valley floor ($6.97 \pm 0.67 \times 10^{10}$ at cm^{-2}). At the

Table 3. Meteoric ^{10}Be Distribution in Bedrock at DC1[a]

Sample Name	Depth Interval (cm)	^{10}Be[b] (atoms/g × 10^7)	Sample Density (g/cm^3)[b]	Inventory (atoms/cm^2 × 10^8)
DC1-1	0–18	16.7 +/− 0.37	5	30.1
DC1-2	18–30	5.01 +/− 0.09	1.8	10.8
DC1-3	30–49	7.18 +/− 0.13	1.8	24.6
DC1-4	49–61	3.43 +/− 0.07	2.6	10.7
DC1-5	61–79	2.34 +/− 0.062	2.6	11
DC1-8	110–120	1.08 +/− 0.052	2.6	2.8
DC1-11	150–170	6.85 +/−0.012	2.6	35.6
DC1-14	240–260	0.1 +/− 0.051	2.6	5.19
DC1-17	340–350	0.27 +/− 0.048	2.6	0.713
DC1-26	610–630	0.58 +/− 0.05	2.6	3.01
DC1-29	1070–1090	2.34 +/− 0.062	2.6	12.2
DC1-32	1520–1540	0.128 +/− 0.043	2.6	0.667
DC1-35	1980–2000	<0.120	2.6	0.312
DC1-37	2290–2300	0.134 +/− 0.048	2.6	0.349

[a]07KNSTD standard used for normalization with assumed ^{10}Be/^{9}Be ratio of 2.85×10^{-12} [*Nishiizumi et al*., 2007]. DC1-##—Deep Core 1, naming convention from *Jin et al*. [2010].

[b]Uncertainty reported represents 1 standard deviation from mean AMS measurement.

[c]Densities estimated from chip densities reported by *Jin et al*. [2010].

Table 4. Meteoric ^{10}Be in North Planar Hillslope Soils[a]

Sample Name	^{10}Be (atoms/g × 10^8)[b]			Depth (cm)	Bulk Density (g/cm^3)[c]	Inventory (atoms/cm^2 × 10^9)		
NPRT0010	7.94	+/–	0.0533	10	1	7.94	+/–	0.0533
NPRT1020	5.42	+/–	0.0818	10	1.4	7.58	+/–	0.1145
NPRT2030	4.65	+/–	0.0299	10	1.8	8.37	+/–	0.0538
NPRT3037	2.39	+/–	0.0429	7	1.8	3.01	+/–	0.0541
NPRT3739	1.28	+/–	0.0115	2	1.8	0.46	+/–	0.0041
NRT1	4.79	+/–	0.0455	22	1.25	13.23	+/–	0.1255
NRT3	6.39	+/–	0.0494	20	1.2	15.34	+/–	0.1186
NRT4	5.08	+/–	0.0509	29	1.39	20.40	+/–	0.2046
NRT5	4.54	+/–	0.0752	29	1.39	18.25	+/–	0.3023
NPUS	5.18	+/–	0.0730	24	1.34	16.84	+/–	4.3784
NPMS0008	10.34	+/–	0.0626	8	1	8.27	+/–	0.0500
NPMS0815	9.52	+/–	0.0581	7	1.4	9.33	+/–	0.0570
NPMS1526	4.55	+/–	0.0293	11	1.8	9.01	+/–	0.0580
NPMS2631	3.67	+/–	0.0259	5	1.8	3.30	+/–	0.0233
NPMS3135	2.85	+/–	0.0236	4	1.8	2.05	+/–	0.0170
NPMS3540	2.41	+/–	0.0200	5	1.8	2.17	+/–	0.0180
NMS1	5.04	+/–	0.0411	31	1.41	22.10	+/–	0.1799
NMS2	5.62	+/–	0.0511	36	1.47	29.65	+/–	0.2695
NMS3	3.50	+/–	0.0423	50	1.56	27.27	+/–	0.3299
NMS4	4.02	+/–	0.0329	32	1.3	16.72	+/–	0.1367
NMS5	3.72	+/–	0.0497	40	1.5	22.29	+/–	0.2980
NPLS	4.98	+/–	0.0386	39	1.49	29.15	+/–	6.9967
NPVF0010	5.70	+/–	0.0463	10	1	5.70	+/–	0.0463
NPVF1020	5.03	+/–	0.0407	20	1.4	7.04	+/–	0.0570
NPVF2028	4.51	+/–	0.0366	8	1.8	6.49	+/–	0.0528
NPVF2836	4.73	+/–	0.0386	8	1.8	6.81	+/–	0.0556
NPVF3644	4.74	+/–	0.0385	8	1.8	6.83	+/–	0.0554
NPVF4449	4.24	+/–	0.0455	5	1.8	3.82	+/–	0.0410
NPVF4957	3.15	+/–	0.0291	8	1.8	4.53	+/–	0.0419
NPVF5764	3.20	+/–	0.0264	7	1.8	4.04	+/–	0.0332
NPVF6470	3.12	+/–	0.0260	6	1.8	3.37	+/–	0.0280
NPVF7074	2.75	+/–	0.0229	4	1.8	1.98	+/–	0.0165
NPVF7478	2.59	+/–	0.0217	4	1.8	1.87	+/–	0.0156
NPVF7885	2.48	+/–	0.0207	7	1.8	3.12	+/–	0.0261
NPVF8588	2.24	+/–	0.0196	3	1.8	1.21	+/–	0.0106
NPVF8891	2.19	+/–	0.0184	3	1.8	1.18	+/–	0.0100
NPVF91103	2.30	+/–	0.0193	12	1.8	4.97	+/–	0.0417
NPVF103115	1.22	+/–	0.0109	12	1.8	2.64	+/–	0.0236
NPVF115118	1.43	+/–	0.0125	3	1.8	0.77	+/–	0.0067
NVF2	3.49	+/–	0.0340	110	1.69	64.85	+/–	0.6329
NVF3	4.57	+/–	0.0442	104	1.68	80.06	+/–	0.7739
NVF4	5.45	+/–	0.0524	81	1.65	72.95	+/–	0.7017
NVF5	4.50	+/–	0.0438	86	1.66	64.30	+/–	0.6258

[a]07KNSTD standard used for normalization with assumed ^{10}Be/^{9}Be ratio of 2.85×10^{-12}. NPRT####—North Planar Ridge Top, depth interval in centimeters. NPMS####—North Planar Mid Slope, depth interval in centimeters. NPVF####—North Planar Valley Floor, depth interval in centimeters.
[b]Uncertainty reported represents 1 standard deviation from mean AMS measurement.
[c]Bulk densities estimated from data reported by *Jin et al*. [2010].

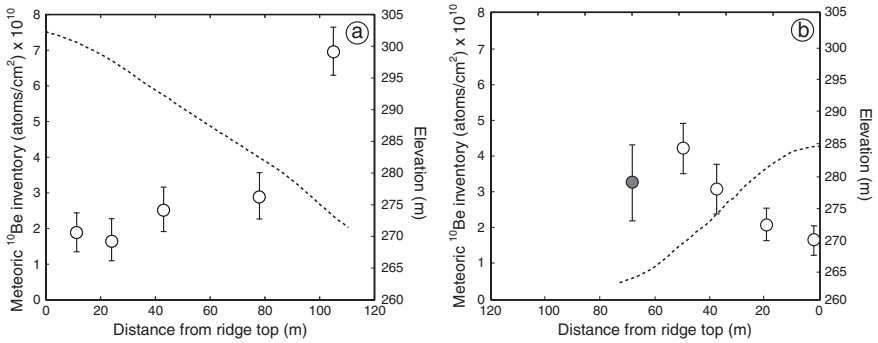

Figure 8. Mean inventories of meteoric ^{10}Be along the (a) north and (b) south hillslopes at SSHO. The error bars indicate 1 standard deviation from the inventory mean at each hillslope position. The SPVF sample location (gray) exhibits a meteoric ^{10}Be inventory considered not to be representative of the total inventory at that location (see text for discussion).

Table 5. Meteoric ^{10}Be in South Planar Hillslope Soils[a]

Sample Name	^{10}Be (atoms/g × 10^8)[b]			Depth (cm)	Bulk Density (g/cm^3)[c]	Inventory (atoms/cm^2 × 10^9)		
SPRT0010	6.6	+/–	0.0779	10	1	6.6	+/–	0.0779
SPRT1020	5.44	+/–	0.0515	10	1.4	7.61	+/–	0.0721
SPRT2030	2.65	+/–	0.0271	10	1.8	4.77	+/–	0.048
SRT1	4.56	+/–	0.0444	25	1.32	15.04	+/–	0.1467
SRT2	4	+/–	0.0389	22	1.25	11.03	+/–	0.1074
SRT3	5.15	+/–	0.0517	30	1.4	21.61	+/–	0.217
SRT4	3.48	+/–	0.0454	30	1.4	14.63	+/–	0.1905
SPUS	4.7	+/–	0.0351	31.2	1.41	20.77	+/–	4.528
SPMS0010	9.62	+/–	0.0909	10	1	9.62	+/–	0.0909
SPMS1020	4.99	+/–	0.0575	10	1.4	6.98	+/–	0.0805
SPMS2030	3.62	+/–	0.0347	10	1.8	6.52	+/–	0.0624
SPMS3040	3.11	+/–	0.045	10	1.8	5.6	+/–	0.081
SPMS4050	2.58	+/–	0.0265	10	1.8	4.64	+/–	0.0477
SPMS5059	2.29	+/–	0.0276	9	1.8	3.71	+/–	0.0497
SMS1	4.86	+/–	0.0333	46	1.54	34.39	+/–	0.2356
SMS2	4.48	+/–	0.0308	32	1.43	20.45	+/–	0.1405
SMS3	3.61	+/–	0.0243	60	1.6	34.69	+/–	0.2334
SMS4	5.03	+/–	0.0336	36	1.47	26.54	+/–	0.1772
SPLS	4.6	+/–	0.0308	57.4	1.59	41.97	+/–	7.019
SPVF0010	5.51	+/–	0.087	10	1	5.51	+/–-	0.087
SPVF1020	3.66	+/–	0.0284	10	1.4	5.12	+/–	0.0397
SPVF2030	4.16	+/–	0.0338	10	1.8	7.49	+/–	0.0609
SPVF3040	2.92	+/–	0.0357	10	1.8	5.26	+/–	0.0643
SPVF4050	3.01	+/–	0.0392	10	1.8	5.42	+/–	0.0705
SPVF5060	2.57	+/–	0.0336	10	1.8	4.63	+/–	0.0605
SPVF6067	2.72	+/–	0.0506	7	1.8	3.43	+/–	0.0912
SVF1	2.48	+/–	0.0249	105	1.69	43.95	+/–	0.4399
SVF2	4.01	+/–	0.0285	60	1.6	38.51	+/–	0.2739
SVF3	3.53	+/–	0.0351	40	1.5	21.17	+/–	0.2106
SVF4	5.01	+/–	0.0394	30	1.4	21.04	+/–	0.1654

[a]07KNSTD standard used for normalization with assumed ^{10}Be/^{9}Be ratio of 2.85×10^{-12}. SPRT####—South Planar Ridge Top, depth interval in centimeters. SPMS####—South Planar Mid Slope, depth interval in centimeters. SPVF####—South Planar Valley Floor, depth interval in centimeters.
[b]Uncertainty reported represents 1 standard deviation from mean AMS measurement.
[c]Bulk densities estimated from data reported by *Jin et al*. [2010].

southern ridge top site, the average meteoric ^{10}Be inventory is $1.63 \pm 0.41 \times 10^{10}$ at cm^{-2}. Inventories increase immediately downslope to $2.08 \pm 0.45 \times 10^{10}$ at cm^{-2}, and continue to increase until the valley floor position from $3.06 \pm 0.69 \times 10^{10}$ at cm^{-2} to $4.20 \pm 0.70 \times 10^{10}$ at cm^{-2}. At the valley floor, however, the average meteoric ^{10}Be inventory decreases to $3.23 \pm 1.06 \times 10^{10}$ at cm^{-2} (Figure 8 and Table 5). As discussed below, we believe this reflects an incomplete sampling (by hand augering) of mobile regolith depth at this locality.

6. Discussion

6.1. Meteoric ^{10}Be in the SSHO Subsurface

[64] The results of our measurements indicate that most meteoric ^{10}Be delivered to the SSHO is retained in the upper decimeters of regolith and does not penetrate deeply into bedrock. As presented by *Jin et al*. [2010], the two uppermost samples from the DC1 core are comprised of regolith from the drill pad site and do not represent bedrock. Excluding these two regolith samples, we find that the inventory of meteoric ^{10}Be from the upper meter of bedrock is ~17% of that retained in ridgetop regolith. This suggests that at SSHO, most of the ^{10}Be delivered by meteoric precipitation is retained in the upper, mobile regolith, and that these inventories can be used to track mobile regolith transport [e.g., *McKean et al*., 1993].

[65] The systematic decrease of ^{10}Be concentrations with depth in hillslope regolith is consistent with addition of meteoric ^{10}Be to the ground surface and efficient ^{10}Be adsorption to mineral surfaces. *Herndon et al*. [2010] reported elevated Mn concentrations in SSHO regolith that are a direct result of industrial inputs via dry fall. The similarity between meteoric ^{10}Be profiles and Mn suggests that both reflect surface addition, with little subsequent physical mixing or geochemical redistribution [*Ma et al*., 2011]. The clay-rich regolith at SSHO [*Lin et al*., 2006; *Jin et al*., 2010] provides high surface area for adsorption [*You et al*., 1989] and thus regolith at SSHO has a relatively high capacity for retaining ^{10}Be. The declining ^{10}Be profiles we observed suggest that regolith is eroding relatively quickly or that SSHO regolith is young and that ^{10}Be has not yet been able to penetrate to greater depth [*Graly et al*., 2010a, 2010b], consistent with the inventories described above.

[66] That these depth-dependent relationships persist at all positions along the hillslope suggests that the mixing rate of mobile regolith is slower than the rate of chemical profile establishment. This conclusion is consistent with those described by *Jin et al*. [2010] for chemical profiles at SSHO and *Kaste et al*. [2007], who observed pronounced ^{7}Be addition profiles in regolith at the Hubbard Brook Experimental Forest, NH, suggesting that physical mixing by bioturbation is limited in New England soils.

6.2. Rates and Duration of Mobile Regolith Transport in the SSHO

[67] Conventional interpretations of cosmogenic isotope concentrations at ridgetops allow for the calculation of

Table 6. Meteoric ^{10}Be Inventory, Residence Time, Erosion Rate, and Flux for North and South Hillslopes at SSHO

Sample Position	Inventory[a] (atoms/cm^2 × 10^{10})	Minimum Residence Time[b] (ky)	Erosion Rate[b] (m/My)	Flux[b] (cm^2/yr)
SPRT	1.63+/−0.41	9.1+/−2.9	19.4+/−6.2	0
SPUS	2.08+/−0.45			5.12+/−1.13
SPMS	3.06+/−0.69			9.88+/−2.17
SPLS	4.20+/−0.70			12.07+/−2.66
SPVF	3.23+/−1.06			-
NPRT	1.89+/−0.55	10.5+/−3.7	16.1+/−5.6	0
NPUS	1.68+/−0.42			6.21+/−1.37
NPMS	2.54+/−0.62			8.02+/−1.76
NPLS	2.92+/−0.73			18.88+/−4.15
NPVF	6.97+/−0.67			31.82+/−7.00

[a]Uncertainties reflect 1 standard deviation from the mean inventory measured at all sites at each hillslope position.
[b]Assuming a meteoric ^{10}Be delivery rate of 1.8×10^6 at cm^{-2} yr^{-1}.

regolith residences times and erosion rates under the assumption of steady regolith thickness [*Brown et al*., 1988, *Portenga and Bierman*, 2011]. Using equation (4) and assuming that the delivery rate of meteoric ^{10}Be has been constant over the recent geologic past at a rate of 1.8×10^6 atoms cm^{-2} yr^{-1} (±20%), a reasonable value for our field site [*Graly et al*., 2010a], the inventories at the north and south ridgetop positions correspond to 10.5 ± 3.7 ky and 9.1 ± 2.9 ky of meteoric ^{10}Be accumulation, respectively (Table 5). Thus, one possible end-member interpretation of the ^{10}Be inventories in ridgetop regolith at SSHO is that they reflect growth and thickening of regolith throughout Holocene time [e.g., *Ma et al*., 2010, 2013]. However, the alternative interpretation of the inventory data is that they reflect steady lowering of the ridgetops while maintaining a constant regolith thickness. In this interpretation, ^{10}Be inventories reflect lowering rates (using equation (5)) of 16.1 ± 5.6 m My^{-1} and 19.4 ± 6.2 m My^{-1} on the north and south ridges, respectively (Table 5). We note that these rates are consistent with the catchment average (~15 m My^{-1}) [*Jin et al*. 2010].

[68] At positions farther downslope, however, it is inappropriate to interpret meteoric ^{10}Be inventories as residence times or lowering rates, as the measured ^{10}Be inventory reflects downslope transport and accumulation of ^{10}Be with creeping mobile regolith [*Monaghan et al*., 1992]. Although downslope increases in ^{10}Be inventories could theoretically develop in immobile regolith of different age, we see no reason to believe that regolith remains in place on SSHO hillslopes (15°–20°) and therefore, the most parsimonious interpretation of downslope increases in ^{10}Be is that they reflect regolith transport [e.g., *McKean et al*., 1993]. Here we use the depth-averaged concentration of meteoric ^{10}Be in mobile regolith to calculate downslope transport rates (equation (26)) [*Monaghan et al*., 1992; *McKean et al*., 1993]. On the northern hillslope, volumetric regolith flux rates increase linearly with position downslope from 6.2 ± 1.4 just below the ridgetop to 31.8 ± 7.0 cm^2 yr^{-1} at the valley floor (Figure 10a). On the southern hillslope, volumetric regolith flux rates increase from 5.1 ± 1.1 just below the ridge top to 12.1 ± 2.7 cm^2 yr^{-1} just upslope of the valley floor (Figure 10b and Table 6).

[69] As noted previously, stratigraphic evidence reveals that SSHO is underlain by coarse colluvial sediment along the sides of the valley floor. The deepest samples from the SPVF profile were likely collected from the colluvial material described as Unit 2. The presence of deep sediments at this position on the southern hillslope suggests that the 67 cm of hand augerable material collected at the south valley floor site is an incomplete sample of the mobile regolith thickness. Thus, the inventory of ^{10}Be we measured at the SPVF site is considered to be a minimum value and excluded from our calculations of regolith flux.

[70] Assuming that creep is the dominant form of regolith transport on hillslopes at SSHO, the differences between the meteoric ^{10}Be inventories at different positions provide an estimate of average velocity (equation (30)). Creep velocities are relatively constant along each hillslope and are similar, within uncertainty, between north and south hillslopes. On the northern hillslope, the measured differences in meteoric ^{10}Be correspond to creep velocities of

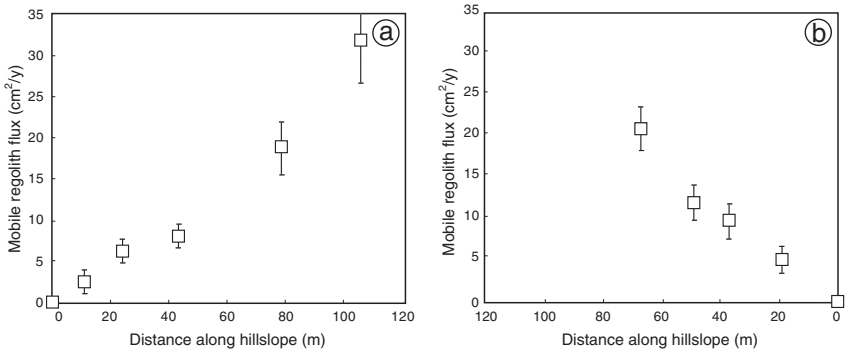

Figure 9. Mean volumetric flux of mobile regolith along the (a) north and (b) south hillslopes of SSHO inferred from meteoric ^{10}Be concentrations measured in hillslope regolith. Error bars reflect 1 standard deviation from the mean regolith flux rate at each hillslope position.

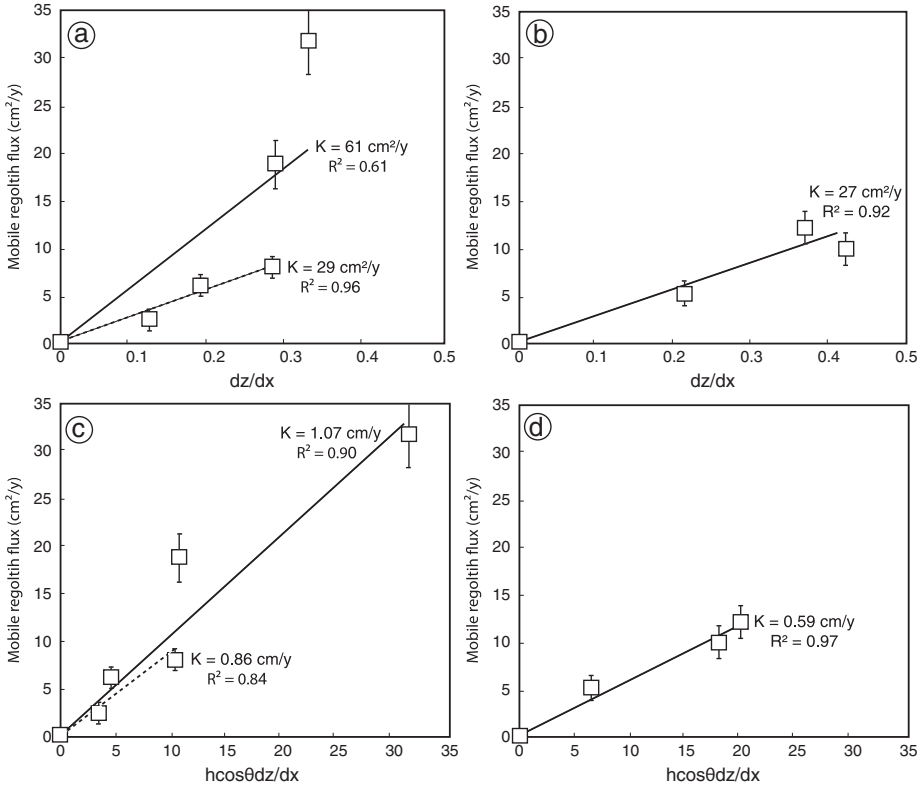

Figure 10. Comparison of regolith flux along the (a) north and (b) south hillslopes with local topographic gradient and with the product of (c) regolith depth and (d) gradient. These results suggest that regolith transport is a function of both depth and hillslope gradient. Fitting only the upper samples on the north hillslope (dashed lines) shows that near the ridgetops, regolith flux is proportional to gradient, and there is less aspect control on transport efficiency (K_1).

0.26 ± 0.08, 0.31 ± 0.10, 0.48 ± 0.15, and 0.27 ± 0.06 cm yr^{-1} for positions sequentially downslope. On the southern hillslope, the creep velocities are similar to those measured on the northern hillslope (within uncertainty) but are slightly lower, at 0.16 ± 0.05, 0.22 ± 0.07, and 0.21 ± 0.07 cm yr^{-1}.

[71] Using depth-averaged regolith densities for each hillslope position, the volumetric fluxes measured on the northern hillslope correspond to increases in mass flux rates from 8.3 ± 1.9 just below the ridge top to 55.0 ± 12.1 g cm^{-1} yr^{-1} at the valley floor. Similarly, the volumetric fluxes measured on the southern hillslope correspond to increases in mass flux rates of 7.3 ± 1.6 to 19.2 ± 4.2 g cm^{-1} yr^{-1}. The mass flux rates presented here are consistent with sediment flux values presented for the southern hillslope by *Jin et al.* [2010], calculated using chemical depletion factors, which increase with position downslope from ~6 to 20 g cm^{-1} yr^{-1}. These sediment fluxes incorporated only material moving by diffusive creep, as particulate loss through pore space was incorporated in the weathering flux values presented by *Jin et al.* [2010]. The consistency between mass flux values calculated using meteoric ^{10}Be and chemical depletion factors provides a compelling argument that meteorically delivered ^{10}Be is moving with mobile regolith particles and is likely not geochemically redistributed in mobile regolith at the SSHO.

[72] Our results suggest that regolith fluxes at SSHO are considerably lower than those inferred from studies of meteoric ^{10}Be accumulation on hillslopes in coastal California [*McKean et al.*, 1993] and in the Smoky Mountains [*Jungers et al.*, 2009]. Bedrock at the Black Diamond Mines Regional Preserve in coastal California is an Eocene marine shale, the hillslopes are of similar gradient to SSHO (~15°), and regolith fluxes range from 52 to 82 cm^2 yr^{-1} [*McKean et al.*, 1993]. Our data imply significantly slower creep velocities (0.2–0.5 cm yr^{-1}) than those in CA (0.9–1.2 cm yr^{-1}) [*McKean et al.*, 1993]. Likewise, creep velocities observed at SSHO are significantly slower than those observed on upland hillslopes of the Flat Creek watershed in the Smoky Mountains (1.2 to 1.7 cm yr^{-1}) reported by *Jungers et al.* [2009]. Hillslopes in the upper section of the Flat Creek watershed also have gradients similar to SSHO (~14°) and are underlain by metamorphosed sandstone. Presumably, the differences observed between SSHO and other field locales are a reflection of the climatic, biologic, and lithologic controls on transport mechanisms and efficiency [e.g., *Perron et al.*, 2009]. Overall, it seems clear that transport velocities and low volumetric fluxes in the SSHO reflect relatively limited transport efficiency at our field site.

7. Implications

7.1. Regolith Transport Rules

[73] Our meteoric ^{10}Be data add to a growing body of work that test rules governing regolith flux on regolith-mantled hillslopes [*McKean et al.*, 1993; *Small et al.*, 1999; *Heimsath et al.*, 2005; *Yoo et al.*, 2007; *Pelletier et al.*, 2011]. The data suggest that, to first order, regolith fluxes at

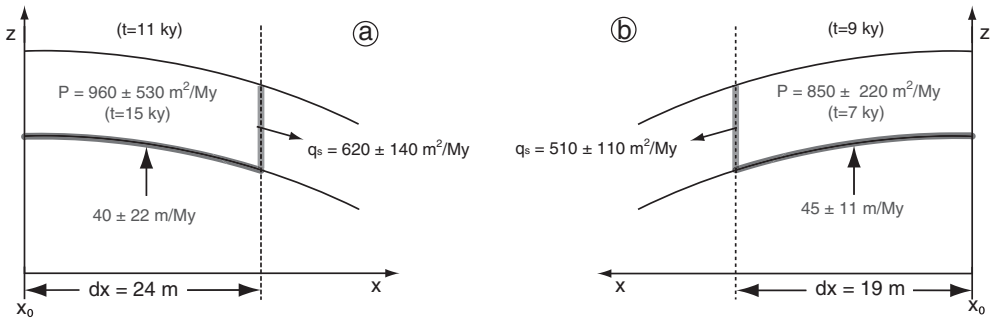

Figure 11. Cartoon summarizing and comparing residence times and fluxes of materials into and out of the (a) north and (b) south ridge tops at SSHO, using U-series and meteoric ^{10}Be. Regolith production rates were calculated using U-series disequilibrium [*Ma et al*., 2010, 2013] and were multiplied by the distance between the ridge crest and the upper slope ^{10}Be sampling positions to estimate the material flux across the bedrock-regolith interface on each ridge. Calculated bedrock-to-regolith fluxes are compared to downslope transport rates inferred from meteoric ^{10}Be. The flux of material from bedrock to mobile regolith calculated using U-series and associated regolith residence times are noted in light gray. The downslope flux rate of mobile regolith calculated using meteoric ^{10}Be and associated regolith residence times are noted in dark gray.

SSHO increase linearly with position downslope (Figure 9). Because hillslope gradients remain relatively constant downslope of the ridgetop, this result also implies that, in general, regolith flux along the north and south hillslopes at SSHO is linearly proportional to the local topographic gradient. Along the first ~40 m downslope from the northern ridge, where regolith is thin, mobile regolith flux is adequately predicted by a linear dependence on local gradient (Figure 10a, $R^2 = 0.96$). On the southern hillslope, regolith flux rates along nearly the entire length of the hillslope are highly correlated to local gradient (Figure 10b), with an R^2 value of 0.92. The transport efficiency (K_1) implied by these data are similar, ranging from 29 ± 5 cm^2 yr^{-1} on the north slope and 27 ± 4 cm^2 yr^{-1} on the south (Figure 10). We note that our data do not preclude the possibility of a nonlinear relationship between regolith flux and local slope [e.g., *Roering*, 2008]. Because topographic gradients at SSHO are relatively gentle, our results do not sample fluxes at gradients approaching thresholds for nonlinearity [*Roering*, 2008].

[74] At the lowest sample positions on the north and south hillslopes at SSHO, where regolith is thickest, however, we observe a departure from a linear dependence of flux on gradient (Figure 10). This observation prompts us to consider whether regolith transport near the valley floor may be better described by a transport rule that depends on both gradient and regolith depth [*Heimsath et al*., 1997; *Gabet et al*., 2003; *Furbish et al*., 2009; *Roering*, 2008]. To test the possibility of a depth-dependent transport rule, we compare fluxes inferred from meteoric ^{10}Be to the product of mobile regolith depth and local gradient (Figures 10c and 10d). Near the northern ridge top, a depth-slope rule provides a slightly poorer fit to regolith flux ($R^2 = 0.84$), relative to the local gradient regression. When the lower two data points are considered, however, a depth-slope rule is a better predictor ($R^2 = 0.90$) than a simple linear dependence on slope. A depth-slope rule is a slightly better predictor of flux on the southern hillslope, with R^2 value 0.97, although we acknowledge that this is not a significant improvement over the simple, slope-dependent rule (Figure 10b). The possibility that a depth-dependent flux rule describes regolith transport at SSHO may reflect a number of possible transport mechanisms, such as freeze-thaw, wetting and drying, and bioturbation. Under these conditions, the magnitude of transport events may be strongly modulated by regolith depth [*Gabet et al*., 2003; *Roering et al*., 2010].

[75] Interestingly, if we consider the implied transport efficiencies for a transport rule that is proportional to the product of regolith depth and gradient, our data hint at a potential difference between the northern and southern hillslopes (Figure 10). The transport coefficient (K_2) along the northern hillslope is greater than that along the southern hillslope (1.1 ± 0.2 and 0.59 ± 0.1 cm yr^{-1}, respectively). This asymmetry suggests that differences in efficiency may be related to topographic aspect [*Ma et al*., 2013] and consequent solar insolation. However, we emphasize that the apparent control of regolith depth on flux rate depends heavily on two data points (Figure 10). Much of our data may be explained by a simple, slope-dependent transport rule with efficiencies that are uniform, at least near the ridge crest. Additional work will be required to determine the range of transport mechanisms, associated transport rules and their distribution in the SSHO.

7.2. Implications for Timescales of Regolith Transport

[76] Our meteoric ^{10}Be data imply that regolith atop ridge crests in the SSHO is relatively young and has developed largely during Holocene time. However, the nature of the valley fill suggests that the SSHO retains a stratigraphic record of transport processes that predate this time period. Although we cannot determine the exact age of the colluvial deposits that underlie the mobile regolith, the ^{14}C age of detrital charcoal from the alluvial material along the valley axis indicates that this material must be older than ~1000 A.D. The depth of the charcoal samples (~30 cm) suggests relatively slow aggradation at SSHO during colonial times; we do not observe significant aggradation as seen elsewhere in the eastern United States [*Walter and Merritts*, 2008]. Thus, if there was significant soil loss during colonial deforestation, the sediment was swept out of the SSHO

catchment. The nature of valley floor sediment below ~30 cm—thick, coarse colluvium—and the position of these deposits largely along the axis of the valley and southern toe slope position are consistent with a periglacial origin and transport [*Clark and Ciolkosz*, 1988; *Braun*, 1989]. Thus, the augerable, mobile regolith (Unit 3) was likely deposited on top of or formed from relict deposits (Units 1 and 2) from a previous time.

7.3. Implications for the Balance Between Regolith Production and Transport

[77] Our study presents a unique opportunity to compare mobile regolith transport rates off ridgetops with independently determined rates of regolith production [*Ma et al*., 2010, 2013; *Jin et al*., 2010]. Mobile regolith residence times at SSHO, calculated using meteoric ^{10}Be and U-series disequilibrium, are similar; on the northern ridge these are 10.5 ± 3.7 (^{10}Be) and 15 ± 8 ky (U-series) [*Ma et al*., 2013], while on the southern ridge these timescales are 9.1 ± 2.9 (^{10}Be) and ~6.7 ky (U-series) [*Ma et al*., 2010].

[78] Although these results suggest that each method is measuring approximately similar regolith residence times, the corresponding regolith production and erosion rates are somewhat different. On the northern ridge top, the mean mobile regolith erosion rate, 16.1 ± 5.6 m My^{-1} (^{10}Be), is approximately half that of the production rate, 39.8 ± 22.3 m My^{-1} (U-series). Similarly, on the southern ridge top, the mobile regolith erosion rate is slower than the production rate at 19.4 ± 6.2 (^{10}Be) and 45 ± 12 m My^{-1} (U-series) [*Ma et al*., 2010, 2013]. Notably, the mean erosion rates appear to be approximately a factor of two lower than regolith production, although we note that rates are within uncertainty of each other (at 2σ). Thus, although our results permit the possibility that regolith production has actually outpaced erosion during the Holocene, within uncertainty regolith production and erosion are in balance along ridgetops in the SSHO.

[79] To allow for direct comparison between our mobile regolith flux results and the regolith production rates reported by *Ma et al*. [2010, 2013], we convert the regolith production rates to volumetric fluxes (Figure 11). We extrapolate the ridge top regolith production rates presented by *Ma et al*. [2010, 2013] across the distances between each ridge top and the corresponding sampling position immediately downslope (i.e., the product of production rate and dx, Figure 11) to estimate volumetric fluxes across the regolith-bedrock interface at the ridge tops. This calculation suggests that the upward fluxes of material transforming from bedrock to regolith per unit width on the northern ridge crest are 960 ± 530 m^2 My^{-1}. The flux of mobile regolith downslope of this position, measured using meteoric ^{10}Be, is $\sim 620 \pm 140$ m^2 My^{-1}. Likewise, on the southern ridge crest, the volumetric flux of material due to weathering is 850 ± 220 m^2 My^{-1}, and the mobile regolith flux downslope is 510 ± 110 m^2 My^{-1} (Figure 11b). Thus, our data indicate that the downslope regolith flux from the north ridge top is 65% of production while that off the south ridge top is ~60% of production. Considering the relatively large uncertainties in our calculations, the production and transport fluxes are within uncertainty of one another. As above, this could be interpreted to imply that regolith production on the SSHO ridge tops has outpaced downslope transport during the Holocene. However, it is also plausible that regolith production and transport may have reached a quasi-steady condition during this time.

[80] To evaluate the potential impact of soil erosion during colonial deforestation [*Walter and Merritts*, 2008], we examine the influence that removal of 10 cm of the upper regolith would have on the meteoric ^{10}Be inventories. We fit an exponential function to the depth profiles at SSHO ridge crests to project the additional inventory represented by additional regolith. This would result in a reduction of estimated erosion rates (~11 m My^{-1}) and lead to an approximate doubling of residence time (~26 ky). Thus, if significant depths of regolith were removed from SSHO ridge crests, this would exacerbate the differences between the calculated rates of regolith production and downslope flux. Thus, although we cannot rule out a role for enhanced erosion in colonial times, we do not find it necessary to explain our results.

[81] It should be noted, however, that the estimated ^{10}Be delivery rate used in our calculations of erosion rate, residence time, and flux does not account for potential inputs via dry fall. If the actual delivery rate, including dry fall, is higher than the value we use, then the erosion rate would be higher than what we report.

8. Conclusions

[82] Our results show that meteoric ^{10}Be is a reliable tracer for mobile regolith flux at SSHO, as it is quantitatively retained in the mobile regolith and not significantly lost to bedrock. Mobile regolith fluxes along hillslopes in the SSHO suggest that over much of the watershed, transport is linearly proportional to the local topographic gradient but that near the valley floor, mobile regolith flux may be a function of both gradient and mobile regolith depth. Additionally, although transport efficiency (K_1) appears to be uniform near north and south ridge crests, we find a potential asymmetry in the rate coefficients for a depth-dependent transport rule (K_2) between north and south hillslopes.

[83] The combination of our results with previous determinations of regolith production rates provides some of the first direct evidence that regolith production and erosion rates are within a factor of two on forested hillslopes in the eastern United States. Given the large uncertainties associated with these data sets, we are presently unable to distinguish whether regolith on ridge crests in the SSHO has reached a steady state or whether regolith is thickening as a response to the climatic shift associated with retreat of the Laurentide ice sheet and the onset of Holocene climate/vegetation. Deep sediments in the valley floor appear to retain a record of enhanced colluvial transport in the recent geologic past and suggest that the present-day, slow creep velocities and low mass flux rates may not be representative of previous conditions at SSHO.

[84] **Acknowledgments.** We would like to thank the anonymous Associate Editor and reviewers, whose suggestions led to improvements in this manuscript. We thank L. Jin and members of the Brantley group for the help in sample collecting and data interpretation. Members of the Cosmogenic Isotope Laboratory at University of Vermont, particularly Luke Reusser, Charles Trodick, and Lee Corbett, provided valuable assistance with meteoric ^{10}Be extractions. N.W. also thanks Jeremy Wimpey for participation in sample collection and sample location surveys. Financial support for this work was provided by the National Science Foundation, grant EAR 07-25019 for the Susquehanna/Shale Hills Critical Zone Observatory to C. Duffy. AMS work was performed under the auspices of the U.S. Department of Energy by Lawrence Livermore National

Laboratory under Contract DE-AC52-07NA27344. NW also acknowledges support from the NASA Earth and Space Science Fellowship Program.

References

Ahnert, F. (1987), Approaches to dynamic equilibrium in theoretical simulations of slope development, *Earth Surf. Processes Landform*, *12*, 3–15.

Aldahan, A., Y. Haiping, and G. Possnert (1999), Distribution of beryllium between solution and minerals (biotite and albite) under atmospheric conditions and variable pH, *Chem. Geol.*, *156*, 209–229.

Amundson, R., D. D. Richter, G. S. Humphreys, E. G. Jobbagy, and J. Gaillardet (2007), Coupling between biota and Earth materials in the critical zone, *Elements*, *3*, 327–332.

Anderson, S. P., F. von Blanckenburg, and A. F. White (2007), Physical and chemical controls on the critical zone, *Elements*, *3*, 315–319.

Bacon, A. R., D. Richter, P. R. Bierman, and D. H. Rood (2012), Coupling meteoric ^{10}Be with pedogenic losses of ^{9}Be to improve soil residence time estimates on an ancient North American interfluves, *Geology*, *40*(9), 1–4, doi:10.1130/G33449.1.

Bierman, P., and E. J. Steig (1996), Estimating rates of denudation using cosmogenic abundances in sediment, *Earth Surf. Processes Landform*, *21*(2), 125–139.

Bierman, P., and J. Turner (1995), ^{10}Be and ^{26}Al evidence for exceptionally low rates of Australian bedrock erosion and the likely existence of pre-Pleistocene landscapes, *Quat. Res.*, *44*(3), 378–382.

Brantley, S. L., and A. F. White (2009), Approaches to modeling weathered regolith, *Rev. Mineral. Geochem.*, *70*, 435–484.

Brantley, S. L., M. B. Goldhaber, and K. V. Ragnarsdottir (2007), Crossing disciplines and scales to understand the critical zone, *Elements*, *3*(5), 307–314.

Braun, D. D. (1989), Glacial and periglacial erosion of the Appalachians, *Geomorphology*, *2*, 233–256.

Brown, L., M. Pavich, R. E. Hickman, J. Klein, and R. Middleton (1988), Erosion of the eastern United States observed with ^{10}Be, *Earth Surf. Processes Landform*, *13*, 441–457.

Brown, E. T., J. M. Edmond, G. M. Raisbeck, D. L. Bourles, F. Yiou, and C. I. Measures (1992), Beryllium isotope geochemistry in tropical river basins, *Geochim. Cosmochim. Acta*, *56*, 1607–1624.

Brown, E. T., R. Stallard, M. C. Larsen, G. M. Raisbeck, and F. Yiou (1995), Denudation rates determined from the accumulation of in situ-produced ^{10}Be in the Luquillo Experimental Forest, Puerto Rico, *Earth Planet. Sci. Lett.*, *129*, 193–202.

Chabaux, F., B. Bourdon, and J. Riotte (2008), U-series geochemistry in weathering profiles, river waters and lakes, *Radioact. Environ.*, *13*, 49–104.

Chadwick, O. A., G. H. Brimhall, and D. M. Hendricks (1990), From a black to a grey box: A mass balance interpretation of pedogenesis, *Geomorphology*, *3*, 369–390.

Ciolkosz, E. J., W. J. Waltman, T. W. Simpson, and R. R. Dobos (1989), Distribution and genesis of soils of the northeastern United States, *Geomorphology*, *2*(1-3), 285–302.

Clark, G. M., and E. J. Ciolkosz (1988), Periglacial geomorphology of the Appalachian highlands and interior highlands south of the glacial border – a review, *Geomorphology*, *1*, 191–220.

Costa, J. E. (1975), Effects of agriculture on erosion and sedimentation in the Piedmont Province, Maryland, *Geol. Soc. Am. Bull.*, *86*, 1281–1286.

Culling, W. E. H. (1963), Soil creep and the development of hillside slopes, *J. Geol.*, *71*(2), 127–161.

Davis, W. M. (1892), The convex profile of bad-land divides, *Science*, *20*, 245.

Dietrich, W. E., D. G. Bellugi, L. S. Sklar, J. D. Stock, A. J. Heimsath, and J. J. Roering (2003), Geomorphic transport laws for predicting landscape form and dynamics, in *Prediction in Geomorphology, Geophys. Monogr. Ser.*, vol. 135, edited by P. Wilcock and R. Iverson, pp. 103–132, AGU, Washington, D. C.

Dixon, J. L., A. M. Heimsath, and R. Amundson (2009), The critical role of climate and saprolite weathering in landscape evolution, *Earth Surf. Processes Landform*, *34*, 1507–1521.

Dosseto, A., B. Bourdon, and S. P. Turner (2008), Uranium-series isotopes in river materials: Insights into the timescales of erosion and sediment transport, *Earth Surf. Processes Landform*, *265*, 1–17.

Dunne, T. (1998), Critical data requirements for prediction of erosion and sedimentation in mountain drainage basins, *J. Am. Water Resour. Assoc.*, *34*(4), 795–808, doi:10.1111/j.1752-1688.1998.tb01516.x .

Fernandes, N. F., and W. E. Dietrich (1997), Hillslope evolution by diffusive processes: The timescale for equilibrium adjustments, *Water Resour. Res.*, *33*(6), 1307–1318.

Fletcher, R. C., H. Buss, and S. L. Brantley (2006), A spheroidal weathering model coupling porewater chemistry to soil thicknesses during steady-state denudation, *Earth Planet. Sci. Lett.*, *244*(1-2), 444–457, doi:10.1016/j.epsl.2006.01.055.

Furbish, D. J., P. K. Haff, W. E. Dietrich, and A. M. Heimsath (2009), Statistical description of slope-dependent soil transport and the diffusion-like coefficient, *J. Geophys. Res.*, *114*, F00A05, doi:10.1029/2009JF001267.

Gabet, E. J. (2003), Sediment transport by dry ravel, *J. Geophys. Res.*, *108*(B1), 2049, doi:10.1029/2001JB001686.

Gabet, E. J., and Mudd, S. M. (2010), Bedrock erosion by tree throw: A model coupling biology and geomorphology to explore the humped soil production function and the persistence of hillslope soils, *J. Geophys. Res.*, *115*, F04005, doi:10.1029/2009JF001526.

Gabet, E. J., O. J. Reichman, and E. W. Seabloom (2003), The effects of bioturbation on soil processes and sediment transport, *Annu. Rev. Earth Planet. Sci.*, *31*, 249–273, doi:10.1146/annurev.earth.31.100901.141314.

Gaillardet, J., B. Dupre, P. Louvat, and C. J. Allegre (1999), Global silicate weathering and CO_2 consumption rates deduced from the chemistry of large rivers, *Chem. Geol.*, *159*, 3–30.

Gallen, S. F., K. W. Wegmann, and D. R. Bohnenstiehl (2013), Miocene rejuvenation of topographic relief in the southern Appalachians, *GSA Today*, *23*, 4–10, doi:10.1130/GSATG163A.1.

Gilbert, G. K. (1909), The convexity of hilltops, *J. Geol.*, *17*, 344–350.

Gosse, J. C., and F. M. Phillips (2001), Terrestrial in situ cosmogenic nuclides: Theory and application, *Quat. Sci. Rev.*, *20*(14), 1475–1560.

Graly, J. A., L. J. Reusser, and P. R. Bierman (2010a), Short and long-term delivery rates of meteoric ^{10}Be to terrestrial soils, *Earth Planet. Sci. Lett.*, *302*(3-4), 329–336, doi:10.1016/j.epsl.2010.12.020.

Graly, J. A., P. R. Bierman, L. J. Reusser, and M. J. Pavich (2010b), Meteoric ^{10}Be in soil profiles – a global meta-analysis, *Geochim. Cosmochim. Acta*, *74*, 6814–6829.

Granger, D. E. (2006), A review of burial dating methods using ^{26}Al and ^{10}Be, in *In Situ-Produced Cosmogenic Nuclides and Quantification of Geologic Processes*, Geologic Society of America Special Paper, edited by L. Siame, D. L. Bourles, and E. T. Brown, vol. *415*, pp. 1–16 .

Hack, J. T. (1960), Interpretation of erosional topography in humid temperate regions, *Am. J. Sci.*, *258A*, 80–97.

Hanks, T. C., R. C. Bucknam, K. R. Lajoie, and R. E. Wallace (1984), Modification of wave-cut and faulting-controlled landforms, *J. Geophys. Res.*, *89*(B7), 5771–5790.

Harden, J. W., T. L. Fries, and M. J. Pavich (2002), Cycling of beryllium and carbon through hillslope soils in Iowa, *Biogeochemistry*, *60*, 317–336.

Heimsath, A. M., W. E. Dietrich, K. Nishiizumi, and R. C. Finkel (1997), The soil production function and landscape equilibrium, *Nature*, *388*(6640), 358–361.

Heimsath, A. M., W. E. Dietrich, K. Nishiizumi, and R. C. Finkel (1999), Cosmogenic nuclides, topography, and the spatial variation of soil depth, *Geomorphology*, *27*, 151–172.

Heimsath, A. M., D. J. Furbish, and W. E. Dietrich (2005), The illusion of diffusion: Field evidence for depth dependent sediment transport, *Geology*, *33*, 949–952.

Heimsath, A. M., R. A. Dibiase, and K. X. Whipple (2012), Soil production limits and the transition to bedrock-dominated landscapes, *Nat. Geosci.*, doi:10.1038/ngo1380.

Herndon, E. M., L. Jin, and S. L. Brantley (2010), Soils reveal widespread manganese enrichment from industrial inputs, *Environ. Sci. Technol.*, *45*(1), 241–247, doi:10.1021/es102001w.

Jin, L., R. Ravella, B. Ketchum, P. R. Bierman, P. Heaney, T. White, and S. L. Brantley (2010), Mineral weathering and elemental transport during hillslope evolution at the Susquehanna/Shale Hills Critical Zone Observatory, *Geochim. Cosmochim. Acta*, *74*, 3669–3691.

Jungers, M. C., P. R. Bierman, A. Matmon, K. Nichols, J. Larsen, and R. Finkel (2009), Tracing hillslope sediment production and transport with in situ and meteoric ^{10}Be, *J. Geophys. Res.*, *114*, F04020, doi:10.1029/2008JF001086.

Kaste, J. M., A. M. Heimsath, and B. C. Bostick (2007), Short-term soil mixing quantified with fallout radionuclides, *Geology*, *35*, 243–246.

Kirkby, M. J. (1971), Hillslope Process-Response Models Based on the Continuity Equation, *Institute of British Geographers Special Publication 3*, 15–30.

Lal, D. (1991), Cosmic ray labeling of erosion surfaces: In situ nuclide production rates and erosion models, *Earth Planet. Sci. Lett.*, *104*, 424–139.

Lal, D., and B. Peters (1967), Cosmic ray produced radioactivity on the earth, in *Handbuch der Physik*, edited by K. Sitte, Springer-Verlag, New York, pp. 551–612 .

Lebedeva, M. I., and S. L. Brantley (2013), Exploring geochemical controls on weathering and erosion on convex hillslopes: Beyond the empirical regolith production function, *Earth Surf. Processes Landform*, doi:10.1002/esp.3424.

Lee, V. E., D. J. DePaolo, and J. N. Christensen (2010), Uranium-series comminution ages of continental sediments: Case study of a Pleistocene alluvial fan, *Earth Planet. Sci. Lett.*, *296*(3-4), 244–254.

Li, S., and C. J. Duffy (2011), Fully coupled approach to modeling shallow water flow, sediment transport, and bed evolution in rivers, *Water Resour. Res.*, *47*, W03508, doi:10.1029/2010WR009751.

Lin, H., W. Kogelmann, C. Walker, and M. A. Bruns (2006), Soil moisture patterns in a forested catchment: A hydropedological perspective, *Geoderma*, *131*, 345–368.

Ma, L., F. Chabaux, E. Pelt, E. Blaes, L. Jin, and S. Brantley (2010), Regolith production rates calculated with uranium-series isotopes at Susquehanna/Shale Hills Critical Zone Observatory, *Earth Planet. Sci. Lett.*, *297*, 211–225.

Ma, L., L. Jin, and S. L. Brantley (2011), Geochemical behaviors of different element groups during shale weathering at the Susquehanna/Shale Hills Critical Zone Observatory, *Appl. Geochem.*, *26*, S89–S93.

Ma, L., F. Chabaux, L. Jin, N. West, E. Kirby, and S. Brantley (2013), Regolith production and transport at the Susquehanna Shale Hills Critical Zone Observatory, part 1: Insights from U-series isotopes, *J. Geophys. Res. Earth Surface*, *118*, 722–740, doi:10.1002/jgrf.20037.

Mackey, B. H., J. J. Roering, and J. A. McKean (2009), Long-term kinematics and sediment flux of an active earthflow, Eel River, California, *Geology*, *37*, 803–806.

Matmon, A., P. R. Bierman, J. Larsen, J. R. Southon, M. J. Pavich, and M. W. Caffee (2003), Temporally and spatially uniform rates of erosion in the southern Appalachian Great Smoky Mountains, *Geology*, *31*(2), 155–158.

McKean, J. A., W. E. Dietrich, R. C. Finkel, J. R. Southon, and M. W. Caffee (1993), Quantification of soil production and downslope creep rates from cosmogenic ^{10}Be accumulations on a hillslope profile, *Geology*, *21*, 343–346.

Meyer, S. C., D. A. Textoris, and J. M. Dennison (1992), Lithofacies of the Silurian Keefer Sandstone, east-central Appalachian basin, USA, *Sediment. Geol.*, *76*, 187–206.

Miller, S. R., P. B. Sak, E. Kirby, and P. R. Bierman (2013), Neogene rejuvenation of central Appalachian topography: Evidence for differential rock uplift from stream profiles and erosion rates, *Earth Planet. Sci. Lett.*, *369 – 370*, 1–12.

Millot, R., J. Gaillardet, B. Dupre, and C. J. Allegre (2002), The global control of silicate weathering rates and the coupling with physical erosion: New insights from rivers of the Canadian Shield, *Earth Planet. Sci. Lett.*, *196*, 83–93.

Molnar, P., Anderson, R. S., and Anderson, S. P. (2007), Tectonics, fracturing of rock, and erosion, *J. Geophys. Res.*, *112*, F03014, doi:10.1029/2005JF000433

Monaghan, M. C., S. Krishnaswami, and K. K. Turekian (1983), ^{10}Be concentrations and the long-term fate of particle reactive nuclides in five soil profiles in California, *Earth Planet. Sci. Lett.*, *65*, 51–60.

Monaghan, M. C., S. Krishnaswami, and K. K. Turekian (1986), The global-average production rate of ^{10}Be, *Earth Planet. Sci. Lett.*, *76*, 279–287.

Monaghan, M. C., J. McKean, W. Dietrich, and J. Klein (1992), ^{10}Be chronometry of bedrock-to-soil conversion rates, *Earth Planet. Sci. Lett.*, *111*, 483–492.

Moulton, K. L., and R. A. Berner (1998), Quantification of the effect of plants on weathering: Studies in Iceland, *Geology*, *26*, 895–898.

Naeser, N. D., C. W. Naeser, C. S. Southworth, B. A. Morgan, and A. P. Schultz (2004), Paleozoic to recent tectonic and denudation history of rocks in the Blue Ridge Province, central and southern Appalachians: Evidence from fission track thermochronology, *Geological Society of America Abstracts with Programs*, *36*, 114.

Naithani, K. J., K. Gaines, D. Baldwin, H. Lin, and D. Eissenstat (2010), Spatial and temporal dynamics of vegetation and hydrological properties at Shale Hills Critical Zone Observatory in Central Pennsylvania, *EOS Trans. AGU*, *91*(52), Fall Meet. Suppl. Abstract. #H53B-1012.

National Oceanographic and Atmospheric Administration (NOAA) (2011), National Oceanic and Atmospheric Administration, National Environmental Satellite Data and Information Service, National Climatic Data Center.

Nishiizumi, K., M. Imamura, M. W. Caffee, J. R. Southon, R. C. Finkel, and J. McAninch (2007), Absolute calibration of ^{10}Be standards, *Nucl. Instrum.Meth. Phys. Res. B*, *258*, 403–413.

Pavich, M. J., L. Brown, and J. N. Vallette-Silver (1985), ^{10}Be analysis of a quaternary weathering profile in the Virginia Piedmont, *Geology*, *1*(1), 39–41.

Pavich, M. J., L. Brown, J. Harden, J. Klein, and R. Middleton (1986), ^{10}Be distribution in soils from Merced River terraces, California, *Geochim. Cosmochim. Acta*, *50*, 1727–1735.

Pelletier, J. D., S. B. Delong, A. H. Al-Suwaidi, M. Cline, Y. Lewis, J. L. Psillas, and B. Yanites (2006), Evolution of the Bonneville shoreline scarp in west-central Utah: Comparison of scarp-analysis methods and implications for the diffusion model of hillslope evolution, *Geomorphology*, *74*, 257–270.

Pelletier, J. D., et al. (2011), Calibration and Testing of Upland Hillslope Evolution Models in a Dated Landscape: Banco Bonito, New Mexico, *J. Geophys. Res.*, *116*, doi:10.1029/2011JF001976.

Perron, J. T., and S. Fagherazzi (2012), The legacy of initial conditions in landscape evolution, *Earth Surf. Process. Landforms*, *37*, 52–63, doi:10.1002/esp.2205.

Perron, J. T., J. W. Kirchner, and W. E. Dietrich (2009), Formation of evenly spaced ridges and valleys, *Nature*, *460*, 502–505.

Portenga, E. W., and P. R. Bierman (2011), Understanding Earth's eroding surface with ^{10}Be, *GSA Today*, *21*(8), 4–10.

Raymo, M. E., and W. F. Ruddiman (1988), Influence of late Cenozoic mountain building on ocean geochemical cycles, *Geology*, *16*, 649–653.

Raymo, M. E., and W. F. Ruddiman (1992), Tectonic forcing of late Cenozoic climate, *Nature*, *359*(6391), 117–122, doi:10.1038/359117a0.

Reimer, P. J. et al. (2004), INTCAL04 terrestrial radiocarbon age calibration, 0–26 cal kyr BP, *Radiocarbon*, *46*(3), 1029–1058.

Reusser, L. J., and P. R. Bierman (2010), Using meteoric ^{10}Be to track fluvial sand through the Waipaoa River basin, New Zealand, *Geology*, *38*, 47–50.

Reusser, L., J. Graly, P. Bierman, and D. Rood (2010), Calibrating a long-term meteoric ^{10}Be accumulation rate in soil, *Geophys. Res. Lett.*, *37*, L19403, doi:10.1029/2010GL044751.

Riebe, C. S., J. W. Kirchner, D. E. Granger, and R. C. Finkel (2001), Strong tectonic and weak climatic control of long-term chemical weathering rates, *Geology*, *29*(6), 511–514.

Riebe, C. S., J. W. Kirchner, and R. C. Finkel (2003), Long-term rates of chemical weathering and physical erosion from cosmogenic nuclides and geochemical mass balance, *Geochim. Cosmochim. Acta*, *67*(22), 4411–4427.

Riebe, C. S., J. W. Kirchner, and R. C. Finkel (2004), Erosional and climatic effects on long-term chemical weathering rates in granitic landscapes spanning diverse climate regimes, *Earth Planet. Sci. Lett.*, *224*(3-4), 547–562.

Roering, J. J. (2008), How well can hillslope evolution models "explain" topography? Simulating soil transport and production with high-resolution topographic data, *GSA Bulletin*, *120*(9-10), 1248–1262.

Roering, J. J., J. W. Kirchner, and W. E. Dietrich (1999), Evidence for nonlinear, diffusive sediment transport on hillslopes and implications for landscape morphology, *Water Resour. Res.*, *35*, 853–870.

Roering, J. J., J. W. Kirchner, and W. E. Dietrich (2001), Hillslope evolution by nonlinear, slope-dependent transport: Steady state morphology and equilibrium adjustment timescales, *J. Geophys. Res.*, *106*(B8), 16,499–16,513.

Roering, J. J., J. Marshall, A. M. Booth, M. Mort, and Q. Jin (2010), Evidence for biotic controls on topography and soil production, *Earth Planet. Sci. Lett.*, *298*(1-2), 183–190.

Rowley, D. B., A. M. Forte, R. Moucha, J. X. Mitrovica, N. A. Simmons, and S. P. Grand (2013), Dynamic topography change of the eastern United States since 3 million years ago, *Science*, doi:10.1126/science.1229180.

Small, E. E., R. S. Anderson, and G. S. Hancock (1999), Estimates of the rate of regolith production using ^{10}Be and ^{26}Al from an alpine hillslope, *Geomorphology*, *27*(1-2), 131–150.

Spotila, J. A., G. C. Bank, P. W. Reiners, C. W. Naeser, N. D. Naeser, and B. S. Henika (2004), Origin of the Blue Ridge escarpment along the passive margin of Eastern North America, *Basin Res.*, *16*, 41–63.

Stallard, R. F., and J. M. Edmond (1983), Geochemistry of the Amazon 2. The influence of geology and weathering environment on the dissolved load, *J. Geophys.*, *88*(NC14), 9671–9688.

Stone, J. (1998), A rapid fusion method for separation of beryllium-10 from soils and silicates, *Geochim. Cosmochim. Acta*, *62*, 555–561.

Swain, F. M. (1966), Distribution of some organic substances in Paleozoic rocks of central Pennsylvania, in *Coal Science*, American Chemical Society, Washington, D.C, pp. 1–21 .

Tucker, G. E., and R. L. Slingerland (1994), Erosional dynamics, flexural isostasy, and long-lived escarpments: A numerical modeling study, *J. Geophys. Res.*, *99*, 12,229–12,243.

Valette-Silver, J. N., L. Brown, M. J. Pavich, J. Klein, and R. Middleton (1986), Detection of erosion events using ^{10}Be profiles: Example of the impact of agriculture on soil erosion in the Chesapeake Bay area (U.S. A.), *Earth Planet. Sci. Lett.*, *80*, 82–90.

Walter, R. C., and D. J. Merritts (2008), Natural streams and the legacy of water-powered mills, *Science*, *319*(5861), 299–304.

West, A. J., A. Galy, and M. Bickle (2005), Tectonic and climatic controls on silicate weathering, *Earth Planet. Sci. Lett.*, *235*(1-2), 211–228.

West, N., E. Kirby, P. R. Bierman, and D. Rood (2011), Preliminary estimates of regolith generation and mobility in the Susquehanna Shale Hills Critical Zone Observatory, PA, using meteoric ^{10}Be, *Appl. Geochem.*, *26*, S146–S148.

Willenbring, J. K., and F. von Blanckenburg (2010a), Long-term stability of global erosion rates and weathering during late-Cenozoic cooling, *Nature*, *465*, 211–214, doi:10.1038/nature09044.

Willenbring, J. K., and F. von Blanckenburg (2010b), Meteoric cosmogenic Beryllium-10 adsorbed to river sediment and soil: Applications for Earth-surface dynamics, *Earth Sci. Rev.*, *98*, 105–122.

Yoo K., R. Amundson, A. J. Heimsath, W. E. Dietrich, and G. H. Brimhall (2007), Integration of geochemical mass balance with sediment transport to calculate rates of soil chemical weathering and transport on hillslopes, *J. Geophys. Res.*, *112*, F02013, doi:10.1029/2005JF000402.

You, C. F., T. Lee, and Y. H. Li (1989), The partition of Be between soil and water, *Chem. Geol.*, *77*, 105–118.